CHAPTER

11

Coastal Ecosystem Modeling in the Context of Climate Change: An Overview With Case Studies

D. Justic[*,1], *S.M. Duke-Sylvester*[§], *J.M. Visser*[§], *Z. Xue*[*], *J. Liang*[*]

[*]Louisiana State University, Baton Rouge, LA, United States and [§]University of Louisiana, Lafayette, LA, United States

[1]Corresponding author: E-mail: djusti1@lsu.edu

OUTLINE

Ecological Model Types, Volume 28
http://dx.doi.org/10.1016/B978-0-444-63623-2.00011-6

11.1 MODELS AS TOOLS FOR ASSESSING THE EFFECTS OF CLIMATE CHANGE ON COASTAL ECOSYSTEMS

Future climatic conditions are expected to include a warmer atmosphere, warmer and more acidic oceans, higher sea levels, and altered precipitation and freshwater discharge patterns, all of which will profoundly influence coastal ecosystems and people living near the coasts. In order to adapt to continuing climate change, it is important to understand how different climatic drivers affect ecosystem processes and species distribution in coastal habitats. Climatic drivers do not act alone but rather in combination with other ecosystem stressors, such as habitat degradation, pollution, eutrophication, and overharvesting of commercially important species. To project ecosystem responses over long temporal and large spatial scales and to separate the influence of climatic drivers from other ecosystem stressors, numerical simulation models have emerged as a major research tool to study the effects of climate change on coastal ecosystems. The complexity and size of these models have been steadily increasing over the past 20 years due to continuing developments in computer technologies and computational techniques but also in response to increased concerns about the sustainability of coastal ecosystems under future climatic conditions.

Numerical models used in the assessment of effect of climate change on coastal ecosystems can be broadly divided into two groups. General circulation models or global climate models (GCMs), such as those featured in the Intergovernmental Panel on Climate Change reports (e.g., IPCC, 2014), are primarily aimed at modeling Earth's climate system at relatively coarse scales (~100 km). In contrast, regional models rely on downscaled GCM products and simulate climate and associated ecosystem processes at much finer scales (~10 km). Numerous regional models have been developed to predict the extent and the potential future effects of climate change on coastal ecosystems, including the rising sea levels (e.g., Craft et al., 2009; McLeod et al., 2010; Storlazzi et al., 2011; Rogers et al., 2012), storm surges (e.g., Wang et al., 2008; Tebaldi et al., 2012), altered precipitation and freshwater discharge patterns (e.g., Najjar et al., 2010; Sperna Weiland et al., 2012; Gochis et al., 2014; Ren et al., 2015), acidification and deoxygenation (e.g., Lerman et al., 2011; Bendtsen and Hansen, 2013), harmful algal blooms (e.g., Glibert et al., 2014), and fisheries impacts (e.g., Hare

et al., 2010; Diamond et al., 2013; Rose et al., 2015; Ruzicka et al., 2016). Many of the models used in climate change impact studies have originally been developed for other applications, e.g., to investigate the influences of specific ecosystem stressors or explain the environmental effects of various human actions and subsequently adapted for climate research applications as regional climate change scenarios became available.

The four case studies presented below discuss modeling studies from ecologically diverse coastal ecosystems of the northern Gulf of Mexico, California Coastal Current system, and the Western Pacific (Fig. 11.1). The approach was not intended to systematically evaluate the use of numerical models in coastal ecosystems but rather to provide examples of how coastal ecosystem modeling is being carried out in the context of climate change.

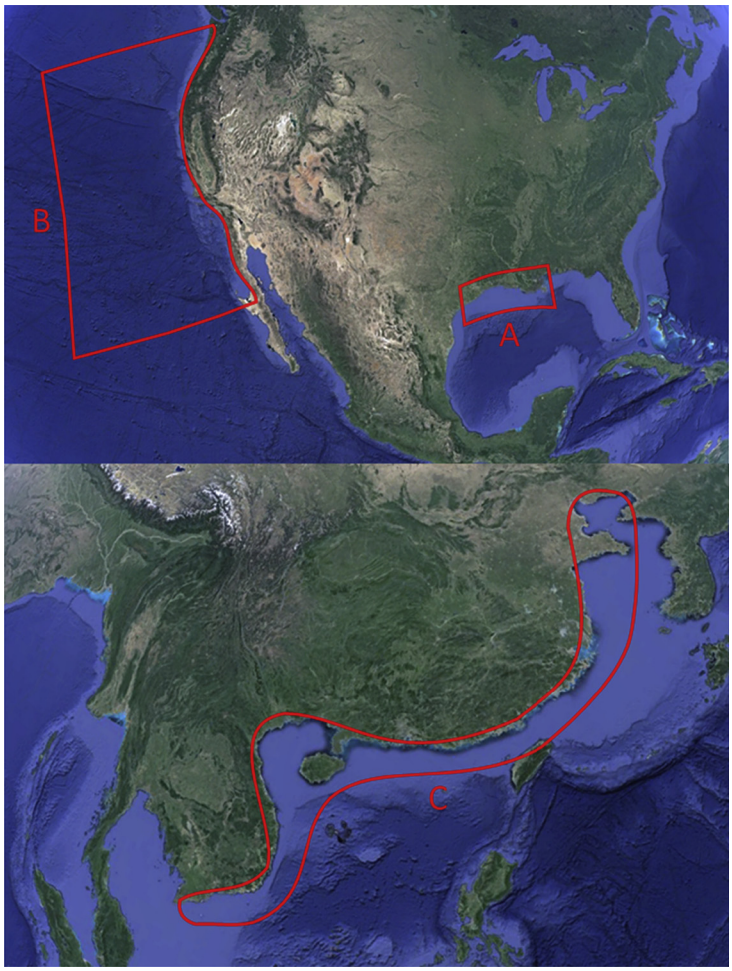

FIGURE 11.1 A map showing the locations of sites in (A) the northern Gulf of Mexico, (B) California Coastal Current system, and (C) the Western Pacific where the selected case studies have been conducted.

11.2 CASE STUDIES

11.2.1 Modeling the Effects of Climate Change on Louisiana's Coastal Wetland Plant Communities

Plant communities play a central role in shaping wetland ecosystems. Both the species composition and plant growth forms define habitat conditions for a diverse collection of arthropods, birds, reptiles, fish, mammals, and a host of other organisms. The plant species that comprise a wetland also shape hydrology and edaphic conditions through processes such as evapotranspiration and frictional resistance to water flow, thus affecting sedimentation and erosion rates. For these reasons, vegetation models are an integral part of ecosystem modeling projects (Craft et al., 2009; Davis and Ogden, 1994; DeAngelis et al., 1998; Peyronnin et al., 2013). The LAVegMod vegetation model is an integral part of a suite of models developed for the Louisiana Coastal Master Plan (LCMP). An earlier version of the model is described in Visser et al. (2013). This section describes an updated and expanded version of the LAVegMod model that is currently used in the development of the 2017 LCMP (Visser et al., 2015). For a more comprehensive view of the overall LCMP modeling effort, see http://coastal.la.gov/a-common-vision/2017-master-plan-update/technical-analysis/.

The objectives of LAVegMod model are twofold. First, it is designed to provide a landscape-scale assessment of potential changes in the response of Louisiana coastal plant communities to natural and anthropogenic perturbations that may occur in coming decades. Second, it is a tool for assessing the effectiveness of management and restoration projects aimed at preserving and enhancing wetlands for their ecological values as well as for sustainable commercial use. This section focuses on the first objective and explores the potential shifts in coastal plant communities in response to various future climate change scenarios.

11.2.1.1 Development and Implementation of the LAVegMod Model

The LAVegMod vegetation model is a component of an integrated compartment model (ICM) that also includes a hydrodynamic box model, a wetland geomorphology model, a barrier island model, and several habitat suitability models. These models are linked together and allow for feedback between the processes captured by each model. The hydrology model simulates the movement of water over the landscape and does so based in part on the distribution of soils and the distribution of plants. Information from the hydrology model is passed to the soil morphology model and the vegetation model. The wetland geomorphology model uses the distribution of water provided, as well as the distribution of plant species, to determine rates of soil accumulation and erosion. The vegetation model receives information from the morphology model about projected additions and/or losses, as well as the distribution of water depth and salinity in space and time provided by the hydrology model, and uses this information to update the distribution of plant species on the landscape.

11.2.1.1.1 MODEL STRUCTURE

The model is spatially explicit and simulates changes in the area covered by each of the 36 plant species (Table 11.1) over time. The species included in our model represent many of the most common dominant plants found in coastal Louisiana. They are associated with the marsh and forest habitats that characterize most of Louisiana's coastland. Each species is

TABLE 11.1 List of Species Included in the LAVegMod Model

Model Type	Habitat	Species	Species Code
Hardwood forest	Bottomland hardwood forest	*Quercus lyrata* Walter	*QULE*
		Quercus texana Buckley	*QUTE*
		Quercus laurifolia Michx.	*QULA3*
		Ulmus americana L.	*ULAM*
		Quercus nigra L.	*QUNI*
		Quercus virginiana Mill.	*QUVI*
Swamp forest	Swamp forest	*Salix nigra* Marshall	*SANI*
		Taxodium distichum (L.) Rich.	*TADI2*
		Nyssa aquatica L.	*NYAQ2*
Floating marsh	Fresh floating marsh	*Panicum hemitomon* Schult.	*PAHE2*
		Eleocharis baldwinii (Torr.) Chapm.	*ELBA2*
		Hydrocotyle umbellata L.	*HYUM*
Emergent marsh	Fresh attached marsh	*Morella cerifera* (L.) small	*MOCE2*
		Panicum hemitomon Schult.	*PAHE2*
		Eleocharis baldwinii (Torr.) Chapm.	*ELBA2*
		Hydrocotyle umbellata L.	*HYUM*
		Sagittaria latifolia Willd.	*SALA2*
		Zizaniopsis miliacea (Michx.) Döll & Asch.	*ZIMI*
		Cladium mariscus (L.) Pohl	*CLMA10*
		Typha domingensis Pers.	*TYDO*
		Schoenoplectus californicus (C.A. Mey.) Palla	*SCCA11*
	Intermediate marsh	*Sagittaria lancifolia* L.	*SALA*
		Phragmites australis (Cav.) Trin. ex Steud.	*PHAU7*
		Iva frutescens L.	*IVFR*
		Baccharis halimifolia L.	*BAHA*
	Brackish marsh	*Spartina patens* (Aiton) Muhl.	*SPPA*
		Paspalum vaginatum Sw.	*PAVA*
	Saline marsh	*Juncus roemeriaunus* Scheele	*JURO*
		Distichlis spicata (L.) Greene	*DISP*
		Spartina alterniflora Loisel.	*SPAL*
		Avicennia germinans (L.) L.	*AVGE*

(*Continued*)

TABLE 11.1 List of Species Included in the LAVegMod Model—cont'd

Model Type	Habitat	Species	Species Code
Barrier Island	Dune	*Uniola paniculata* L.	*UNPA*
		Panicum amarum Elliott	*PAAM2*
		Sporobolus virginicus (L.) Kunth.	*SPVI3*
	Swale	*Spartina patens* (Aiton) Muhl.	*SPPABI*
		Distichlis spicata (L.) Greene	*DISPBI*
		Solidago sempervirens L.	*SOSE*
		Strophostyles helvola (L.) Elliott	*STHE9*
		Baccharis halimifolia L.	*BAHABI*
Submerged aquatic vegetation	Water		*SAV*

characterized by the environmental conditions that allow its establishment and persistence. The model also includes the information on the conditions that may lead to plant senescence.

The spatial domain of the model is the entire Louisiana coast, extending from the Texas border to the Mississippi border. The southernmost extent of the model falls within the Gulf of Mexico and is located at approximately the 30 m isobath which corresponds to a distance between 40 and 100 km from the coast (Fig. 11.2). This domain was selected so that the hydrology along the border was no longer influenced by freshwater and estuarine processes.

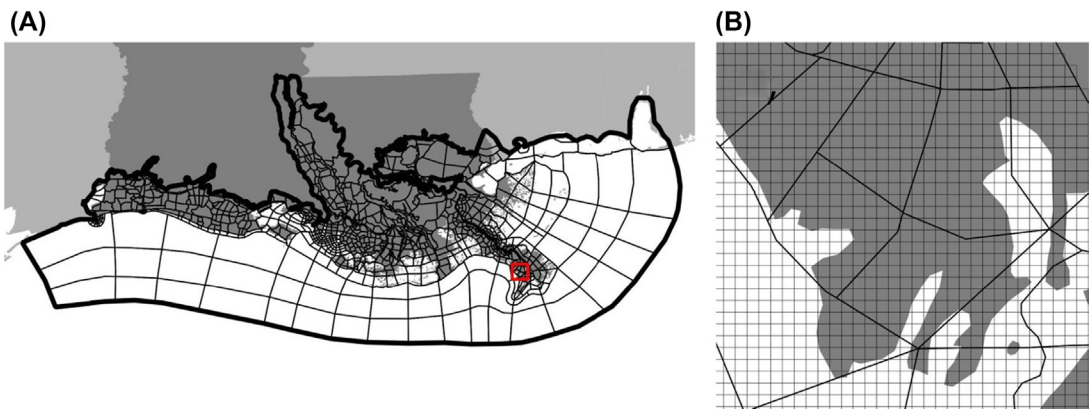

FIGURE 11.2 (A) The spatial domain of the LAVegMod model. Gray areas denote land, with Louisiana shown in dark gray and the neighboring Gulf coast states shown in lighter gray. The heavy black line denotes the overall model domain. The partitions used by the hydrology model are shown as thinner black lines. The red box shows the location and extent of the area show in panel B. (B) A subset of the model domain. Areas that are wetland marshes are shown in gray and open water areas are shown in white. The irregular polygons are the boxes used by the hydrology model. The regular lattice is the 500 × 500 m grid used by the vegetation model.

Instead the hydrology dynamics at the southern boundary are primarily driven by tidal and wave processes. The northern boundary of the model was selected to correspond to the 10 m elevation contour with the Atchafalaya basin drainage added up to the stream flow gage located at Simmesport, Louisiana (Fig. 11.2).

The 48,722 km^2 spatial domain is divided into a structured grid composed of 500 × 500 m cells. Within each cell, the model only tracks the fraction of the area that is covered by each species as well as the area that is covered by water. The model does not track the spatial structure of species within a cell.

The temporal domain of the model is a 50-year planning horizon. The model updates the plant species distributions at the end of the growing season (October) on a yearly time step. In each time step, the fraction of each plot that is covered by each species is evaluated and updates in the vegetation cover are performed on a plot-by-plot basis. Changes in the vegetation cover within a plot are based on the local hydrology and morphology, as well as on the range of hydrologic conditions each species can tolerate and dispersal of propagules from neighboring locations.

The 36 plant species are grouped into six functional groups that are represented by different vegetation submodels: emergent wetlands, hardwood forest, swamp forest, floating marsh, submerged aquatics (SAV), and barrier island vegetation (Table 11.1). For each species, the probability of establishment and senesce are specified. At each time step, the model uses this information in a two-step process. In the first step, the model computes the probability of senescence for each species based on the hydrology and salinity conditions. The cover of each species within a cell is decreased in proportion to its probability of senescence. The reduction in cover of species i within a plot is calculated as:

$$C_i'(t+1) = \left[1 - P_{senescence,i}\{H(t), S(t)\}\right] C_i(t) \tag{11.1}$$

where t is time, $C_i(t)$, is the cover of species i at time t, $H(t)$ is local hydrology conditions, $S(t)$ is salinity, $P_{senescence,i}\{H(t),S(t)\}$ is the probability of senescence under the local hydrology and salinity conditions and $C_i'(t+1)$ is the cover of species i at time $t+1$ after the effects of senescence have been assessed, but before the effects of establishment have been assessed. The $H(t)$ and $S(t)$ values are different for different functional groups and are defined in the description of each submodel. The location index is not included in the above notation to minimize the notational clutter. However, Eq. (11.1) is applied to each 500 × 500 m cell of the model, where $H(t)$, $S(t)$, $C_i(t)$ and $C_i'(t+1)$ represent local quantities for each cell.

The second model step is used to determine what species become established in any open area within a plot. The open area within a plot consists of the area made vacant by the senescing of species from the first step plus any area that was not previously occupied. The available area is divided among the species in proportion to their probability of establishment under the local hydrology and salinity conditions. Establishment is also governed by the ability of species to disperse from the area surrounding each 500 × 500 m cell. The increase in area covered by species i is evaluated as:

$$C_i(t+1) = \left[\left(A - \sum_{j=1}^{K} C_j(t)\right) + \sum_{j=1}^{K}\left\{C_j(t) - C_j'(t+1)\right\}\right] \frac{P_{establish,i}(H(t), S(t))P_{disp,i}}{\sum_{j=1}^{K} P_{establish,j}(H(t), S(t))P_{disp,j}} \tag{11.2}$$

where t is time, and i and j are species indices. A is the total area in the plot, $C_j(t)$ is the cover of species j, the sum of $C_j(t)$ is the total area covered by species at time step t, and the difference of this sum and A is the area that was unoccupied at time t. $C'_j(t+1)$ is the cover of species j after the effects of senescence have been assessed, the difference between $C_j(t)$ and $C'_j(t+1)$ is the area lost by species j, and the sum of these differences is the total area vacated as a result of senescence. The sum of the first two terms on the right-hand side is the total area that is unoccupied and is available for species to become established. This quantity is multiplied by the relative probability of establishment by species i, where $P_{establish,i}(H(t),S(t))$ is the probability of species i becoming established under conditions, $H(t)$ and $S(t)$. $P_{disp,i}$ is the probability of species i dispersing into the local patch from the surrounding area. The product of $P_{establish,i}$ and $P_{disp,i}$ is normalized by the total probability of establishment summed over all species. As in Eq. (11.1), the spatial indexing is omitted to make the equation more readable. The probability of dispersing into a plot by species i ($P_{dist,i}$) varies according to the description of each species group as different groups of species are adapted to different hydrology and salinity conditions.

11.2.1.1.2 EMERGENT WETLANDS

The model includes 20 species that represent emergent wetlands (Table 11.1). Included in this list are species that are among the most common inhabitants of freshwater, intermediate, brackish, and saline marshes. For these species, the environmental conditions that govern establishment and senescence are the annual standard deviation in water depth, $H(t) = H_{stdev}(t)$ and the annual mean salinity, $S_{mean}(t)$. The probability of senescence, $P_{senescence,i}(H_{stdev}(t),S_{mean}(t))$ is a bivariate function obtained by applying bilinear interpolation to a table of probabilities. The probability of establishment, $P_{establish,i}(H_{stdev}(t),S_{mean}(t))$, is also obtained by applying bilinear interpolation to a table of probabilities (Table 11.2).

The use of annual mean salinity and the annual standard deviation in stage height as the factors defining a species niche was developed through an analysis of the data collected by the Coast-wide Reference Monitoring System (CRMS) (Folse et al., 2012; Visser et al., 2015). There are over 350 CRMS monitoring stations distributed throughout Louisiana's coastal wetlands, with most stations having collected data from 2009 to the present. Data from these stations include continuous monitoring of environmental parameters including stage height, salinity, water temperature, and air temperature. CRMS data also include annual surveys of vegetation cover. We used this data to estimate the niche width of each of our emergent wetland species with respect to a number of potential factors including hydroperiod, annual mean and median water depth, and salinity. Salinity and the standard deviation in water depth were the only two factors where different species showed different niche ranges (Snedden and Steyer, 2013). Salinity is a well-known factor governing the distribution of coastal wetland species (Mitsch and Gosselink, 2000; Baldwin and Batzer, 2012) and its inclusion here reflects the stress that plants experience in the presence of saltwater and the adaptations some mesohaline and polyhaline species have evolved.

The standard deviation in water depth is a less obvious factor distinguishing species. This factor was used as a measure of the rate of nutrient exchange where areas with high variation in stage experience rapid exchange and frequent replenishment of nutrients while areas with low variation in stage are nutrient limited. This factor also reflects the differential responses

TABLE 11.2 Probability of establishment of *Spartina patens* as a function of annual mean salinity and standard deviation in stage height

	Water level variability																				
Salinity	**0**	**0.04**	**0.08**	**0.12**	**0.16**	**0.2**	**0.24**	**0.28**	**0.32**	**0.36**	**0.4**	**0.44**	**0.48**	**0.52**	**0.56**	**0.6**	**0.64**	**0.68**	**0.72**	**0.76**	**10**
0	0	0	0	0	0	0	0	0	0	0	0	0	0	0	0	0	0	0	0	0	0
0.2	0	0	0	0	0	0	0	0	0	0	0	0	0	0	0	0	0	0	0	0	0
0.4	0	0	0	0	0	0	0	0	0	0	0	0	0	0	0	0	0	0	0	0	0
0.6	0	0	0	0	0	0	0	0	0	0	0	0	0	0	0	0	0	0	0	0	0
0.8	0.1	0.2	0.3	0.05	0.1	0.1	0.1	0.05	0	0	0	0	0	0	0	0	0	0	0	0	0
1	0.2	0.3	0.4	0.2	0.25	0.3	0.25	0.15	0.1	0.05	0	0	0	0	0	0	0	0	0	0	0
1.2	0.3	0.4	0.5	0.35	0.4	0.4	0.4	0.35	0.3	0.25	0.2	0.1	0.05	0	0	0	0	0	0	0	0
1.4	0.4	0.5	0.6	0.5	0.55	0.6	0.55	0.5	0.45	0.4	0.4	0.3	0.25	0.15	0.1	0.05	0	0	0	0	0
1.6	0.5	0.6	0.7	0.65	0.7	0.7	0.7	0.65	0.6	0.55	0.5	0.45	0.4	0.35	0.3	0.25	0.15	0.1	0.05	0	0
1.8	0.6	0.7	0.8	0.8	0.85	0.9	0.85	0.8	0.75	0.7	0.7	0.55	0.5	0.45	0.4	0.35	0.3	0.25	0.2	0.15	0
2	0.7	0.8	0.9	0.95	1	1	1	0.95	0.9	0.85	0.8	0.75	0.7	0.65	0.55	0.5	0.45	0.4	0.35	0.3	0
3	0.7	0.8	0.9	0.95	1	1	1	0.95	0.9	0.85	0.8	0.75	0.7	0.65	0.55	0.5	0.45	0.4	0.35	0.3	0
4	0.7	0.8	0.9	0.95	1	1	1	0.95	0.9	0.85	0.8	0.75	0.7	0.65	0.55	0.5	0.45	0.4	0.35	0.3	0
5	0.7	0.8	0.9	0.95	1	1	1	0.95	0.9	0.85	0.8	0.75	0.7	0.65	0.55	0.5	0.45	0.4	0.35	0.3	0
6	0.5	0.6	0.7	0.75	0.8	0.8	0.8	0.75	0.7	0.65	0.6	0.55	0.5	0.45	0.4	0.35	0.3	0.25	0.15	0.1	0
7	0.3	0.4	0.5	0.55	0.6	0.6	0.6	0.55	0.5	0.45	0.4	0.35	0.3	0.25	0.15	0.1	0.05	0	0	0	0
8	0.1	0.2	0.3	0.35	0.4	0.4	0.4	0.35	0.3	0.25	0.2	0.15	0.1	0.05	0	0	0	0	0	0	0
9	0	0	0.1	0.15	0.2	0.2	0.2	0.15	0.1	0.05	0	0	0	0	0	0	0	0	0	0	0
10	0	0	0	0	0	0	0	0	0	0	0	0	0	0	0	0	0	0	0	0	0
12	0	0	0	0	0	0	0	0	0	0	0	0	0	0	0	0	0	0	0	0	0
14	0	0	0	0	0	0	0	0	0	0	0	0	0	0	0	0	0	0	0	0	0
100	0	0	0	0	0	0	0	0	0	0	0	0	0	0	0	0	0	0	0	0	0

For intermediate values of salinity and standard deviation in stage height, the probability is calculated based on linear interpolation of the nearest neighboring values.

of species to nutrient availability, with some species being adapted to nutrient stress and others being adapted to take advantage of available nutrients.

Propagules of emergent wetland species disperse into a cell in proportion to the fraction of area covered by a species in the neighboring cells. The probability of species i dispersing its propagules into a given cell is evaluated based on the average cover in the neighboring cells:

$$P_{dist,i} = \frac{1}{N}\sum_{k=1}^{N} C_i(t;k) \tag{11.3}$$

where k is the location index for the neighbors. The number of neighbors varies from 1 to 8, depending whether a cell is on the border of the model domain or is situated in the interior. Note that the number of neighboring cells can be less than three because the model domain is not rectilinear. If species i completely covers the surrounding neighboring cells, i.e., $C_i(t;k) = 1$ for all k, then $P_{dist,i}$ is also equal to 1. In all other cases $P_{dist,i}$ is smaller than 1.

11.2.1.1.3 HARDWOOD FOREST

Six of the species included in our model represent hardwood forest species. These are primarily oak species that commonly grow near the coast but the forest group also includes American elm (*Ulmus americana*) (Table 11.1). The probability that a hardwood species will become established depends on the duration of flooding within the year, the elevation of the land above annual mean stage height, and salinity. For these species, salinity ($S(t)$) is expressed as the annual average salinity. Hydrology is summarized in two ways for hardwood species, as an index of flooding conditions, $H_{flood}(t)$, and as the land elevation above the annual mean stage height, $H_{height}(t)$.

In order for seedlings to become established, there must be a continuous two-week period with no surface water present, followed immediately by a two-week period where the water never exceeds 0.1 m in depth. These criteria are common to all six of the hardwood species we have included. The equation for the flooding index is:

$$H_{flood}(t) = \begin{cases} 1 & H_{daily}(d) < 0 \quad \text{for} \quad d = d_0 \ldots d_0 + 15 \\ & \text{and} \\ & H_{daily(d)} < 10 \text{ cm} \quad \text{for} \quad d = d_0 + 15 \ldots d_0 + 29 \\ & \text{for any } d_0 \text{ in year } t \\ 0 & \text{otherwise} \end{cases} \tag{11.4}$$

where d and d_0 denote time in days within a year t and $H_{daily}(d)$ is the stage height relative to land surface elevation (e.g., $H_{daily}(d) < 0$ indicates subsurface water).

The probability of establishment is calculated as:

$$P_{establish,i}(H_{height}(t), H_{flood}(t), S(t)) = \begin{cases} P_{elv,i}(H_{height}(t)) & \text{if } S(t) < 1 \text{ ppt} \quad \text{and} \quad H_{flood}(t) = 1 \\ 0 & \text{otherwise} \end{cases} \tag{11.5}$$

where t is time in years. In Eq. (11.5), $P_{elv,i}(H_{height}(t))$ is the probability of establishment for species i expressed as a function of the annual average height of the ground above the water surface, $H_{height}(t)$. The establishment probability is a piecewise linear function whose shape is parameterized by a table of values relating elevation to establishment probability (Table 11.3). *Quercus lyrata*, *Quercus texana*, and *Quercus laurifolia* occupy the lowest range of elevations, followed by *U. americana*, *Quercus nigra*, and finally *Quercus virginiana* at the highest elevations.

Senescence conditions are based on annual average salinity ($S(t)$) and land elevation above annual mean stage height, $H_{height}(t)$:

$$P_{senescence,i}(H_{height}(t),\ S(t)) = \begin{cases} P'_{senescence,i}(H_{height}(t)) & \text{if } S(t) < 1 \text{ ppt} \\ 1 & \text{otherwise} \end{cases} \tag{11.6}$$

TABLE 11.3 Probability of Establishment for Six Selected Upland Forest Species

Elevation (m)	*Quercus lyrata*	*Quercus texana*	*Quercus laurifolia*	*Ulmus americana*	*Quercus nigra*	*Quercus virginiana*
−0.1525	0	0	0	0	0	0
0	0.1	0.1	0.1	0	0	0
0.1525	0.2	0.2	0.2	0	0	0
0.305	0.3	0.3	0.3	0.1	0.1	0
0.475	0.4	0.4	0.4	0.2	0.2	0
0.61	0.7	0.7	0.7	0.3	0.3	0
0.7625	0.8	0.8	0.8	0.4	0.4	0
0.915	1	1	1	0.6	0.6	0.2
1.0675	1	1	1	0.7	0.7	0.4
1.22	0.8	0.8	0.8	1	1	0.6
1.3725	0.7	0.7	0.7	1	1	0.8
1.525	0.4	0.4	0.4	0.6	0.6	1
1.6775	0.2	0.2	0.2	0.4	0.4	1
1.83	0	0	0	0.2	0.2	1
1.9825	0	0	0	0.1	0.1	1
2.135	0	0	0	0	0	1

where $P'_{senescence,i}(H_{height}(t))$ is the probability of senescence for species i. $P'_{senescence,i}(H_{height}(t))$ is a piecewise linear function obtained by applying linear interpolation to parameters in Table 11.3. The conditions defined by the establishment table are the opposite of those for senescent. For example, *Q. lyrata*, *Q. texana*, and *Q. laurifolia* will begin to senesce if the elevation above mean water height either exceeds 1.22 m or falls below 0.76 m.

The establishment tables for these species were derived based on the literature data on the distribution of these species along the elevation gradient (Wall and Darwin, 1999; Denslow and Battaglia, 2002; Natural Resource Professionals, 2001; Theriot, 1993).

11.2.1.1.4 SWAMP FOREST

The model includes three swamp forest species, *Salix nigra*, *Taxodium distichum*, and *Nyssa aquatica* (Table 11.1). Senescence for these species is described in the same way as for the emergent wetland species. The environmental conditions that govern senescence and establishment are the annual standard deviation of stage height ($H(t)$) and the annual mean salinity ($S(t)$). The probability of senescence, $P_{senescence,i}(H(t),S(t))$, is a function obtained by applying bilinear interpolation to a table of probabilities. The establishment tables for these species are also based on the analysis of the CRMS data (Visser et al., 2015).

The establishment model for swamp forest species is based on annual mean salinity, $S(t)$, and on two summaries of the hydrology data: the annual standard deviation in water depth, $H_{stdev}(t)$, and the flooding index used for the upland hardwood species, $H_{flood}(t)$. The probability of establishment is calculated as:

$$P_{establish,i}(H_{stdev}(t),\ H_{flood}(t), S(t)) = \begin{cases} P'_{establish,i}(H_{stdev}(t), S(t)) & \text{if} \quad H_{flood}(t) = 1 \\ 0 & \text{otherwise} \end{cases} \tag{11.7}$$

where $P'_{establish,i}(H_{stdev}(t), S(t))$ is a function obtained by applying bilinear interpolation to a species-specific probability table similar to Table 11.2. Dispersal for the swamp forest species is evaluated in the same way as described for the emergent wetland species (Eq. (11.3)).

11.2.1.1.5 FLOATING MARSH

Our model includes three floating marsh species (Table 11.1). Floating marshes form when soils within the rooting zone of the plants become detached from lower soil strata and the resulting vegetation mat becomes buoyant (Sasser et al., 1996). In Louisiana, these marshes are typically associated with three emergent wetland species, *Panicum hemitomon*, *Eleocharis baldwinii*, and *Hydrocotyle umbellata.* These species are already included in the model and are modeled using the emergent wetlands model described above. They are grouped as a separate model category because floating marshes in which these species dominate are the result of different processes and have a different fate when they senesce. The formation of these marshes is thought to take place on a much slower time scale than the 50-year time horizon used in this model. For this reason, the model does not include an establishment process for these species and so $P_{establish,i}(H(t),S(t)) = 0$ for all three emergent wetland species. The initial distribution of floating marsh is determined by the model's initial conditions and the marsh can only experience senescence during a simulation. Senescence of floating marshes is governed by the same rules as used for the emergent wetland species and so the senescence table for each of the species associated with floating marshes is the same one used for the emergent wetland species.

When floating marshes senesce, the area they previously occupied becomes open water. This is different from the emergent marshes, where area lost by one emergent marsh species can be reoccupied by another species. The floating mat of soil and plants is often separated from the soil surface by a half a meter or more of water (Sasser et al., 1996). If a floating marsh is destroyed, the resulting water is too deep for emergent species to become established and the area becomes open water. The floating marshes are included in the model to capture this process and the location and extent of open water created by the death of floating marsh is communicated to the hydrology and soil morphology models that are linked to the LAVegMod model.

11.2.1.1.6 SUBMERGED AQUATICS

Submerged aquatic vegetation (SAV) is a common feature in Louisiana's wetlands. SAV can influence hydrology by increasing surface friction and soil morphology as they stabilize soils with their roots. In the LAVegMod model, SAV is the only plant category that is not modeled at the species level. The model uses a different set of summaries of hydrology and salinity to estimate cover. This approach is dictated by the limited availability of data for the

SAV species that occupy Louisiana's wetlands. For example, the CRMS data set that was the basis for our emergent wetlands parameters does not include SAV species.

The SAV model is based on a linear regression that relates the cover of SAV to summer mean water depth, water temperature, and salinity (Visser et al., 2013):

$$C_{SAV}(t) = C_{Water}(t)\left[1.83 - 3.7 \times 10^2\, T_{summer}(t) - 7.7 \times 10^2\, S_{summer}(t) - 2.6 \times 10^2\, H_{summer}(t)\right] \quad (11.8)$$

where $C_{water}(t)$ is the fraction of a cell covered by water in year t, $T_{summer}(t)$, $S_{summer}(t)$, and $H_{summer}(t)$ are the summer mean water temperature, summer mean salinity, and the summer mean water depth in year t, respectively.

11.2.1.1.7 BARRIER ISLAND VEGETATION

The model includes eight species that are commonly found on Louisiana's coastal barrier islands. Three of these species are also included in our emergent wetland species (*Baccharis halimifolia*, *Spartina patens*, and *Distichlis spicata*). We include these species separately for the barrier islands because different processes govern their establishment and senescence on barrier islands. The remaining five species are typically found only on Louisiana's barrier islands.

The establishment of barrier island species is determined by height above mean sea level. Height above mean sea level is a proxy for a number of related factors, including exposure to salt from sea spray, exposure to scouring from wind, and exposure to tidal energy and inundation. Low elevation areas are exposed to high wave energy, frequent inundation, high salinity, and relatively low scouring from wind. As elevation increases wave energy and inundation decrease because these locations are farther from the shore, salinity decreases because rain water tends to flush salts downhill, and scouring from wind increases as plants become more exposed. The cumulative effect of these processes is such that each species is found only within a characteristic band at a distinctive elevation above the shoreline. The probability of establishment is a piecewise linear function of elevation that is obtained by applying linear interpolation to a species-specific probability table similar to Table 11.2.

11.2.1.2 Model Inputs

The vegetation model takes input from a hydrology model and a soil morphology model. The hydrology model provides daily estimates of water stage height, salinity, and water temperature for the entire model domain at a 500 × 500 m resolution. This information is then summarized into the annual and summer season statistics required by the various submodels (Table 11.4). The model also records a map of this distribution of land and water from the soil morphology model. This map is updated every year, noting the fraction of each 500 × 500 m cell that is classified as land and the fraction classified as open water for the entire model domain. This map is used to determine where plants can become established. Only the portion of each cell that is classified as "land" can be occupied by terrestrial species, while only areas classified as "open water" can be occupied by SAV. These quantities are updated by the soil morphology model based on changes in hydrology, the transport of sediments, and the distribution of plants. At the start of each yearly time step, the vegetation model updates the cover of plants in each 500 × 500 m cell to reflect the input from the soil morphology

TABLE 11.4 Hydrology and Soil Morphology Model Inputs to the LAVegMod Submodels

Input	Description	LAVegMod Submodels
$H_{flood}(t)$	Index of flooding used for tree establishment	Hardwood forests
		Swamp forest
$H_{height}(t)$	Height of land surface above mean water surface	Hardwood forests
		Barrier islands
$H_{stdev}(t)$	Annual standard deviation in stage height	Emergent wetlands
		Swamp forest
$S(t)$	Annual mean salinity	Hardwood forest
		Swamp forest
		Emergent wetlands
$T_{summer}(t)$	Summer mean water temperature	Submerged aquatic vegetation
$S_{summer}(t)$	Summer mean salinity	Submerged aquatic vegetation
$D_{summer}(t)$	Summer mean water depth	Submerged aquatic vegetation

model. If a cell experiences no change in the proportion of land and water, there is no adjustment needed to the plant species cover. If the soil morphology model predicts an increase in land fraction (and a corresponding decrease in water fraction), the model computes the difference between the area currently covered by plants and the area of "new" land provided by the soil morphology model. The difference is classified as unoccupied and will be included in the next update of the vegetation dynamics.

If the soil morphology model predicts a reduction in the fraction of a cell that is covered by land, the reduction in the cover of terrestrial species is computed as:

$$C_i'(t) = C_i(t)\frac{L(t)}{\sum C_i(t)} \tag{11.9}$$

where $L(t)$ is the new fraction of a cell predicted to be land by the soil morphology model and the sum of the loss is taken over all terrestrial plant species (i.e., all species but SAV). $C_i'(t)$ is the cover of species i after the adjustment, which is subsequently used to update cover based on hydrology and salinity (Eqs. (11.1) and (11.2)).

The initial conditions for the model are based on a habitat classification map formulated from satellite telemetry data for the year 2010. The map provides individual species cover for each 30 × 30 m cell. This information is then converted into a coarser 500 × 500 m map that is used in the LAVegMod model.

11.2.1.3 Climate Change Scenarios

We considered three hypothetical climate change scenarios (Table 11.5). All three scenarios assume increased flooding, both in extent and duration, and associated increases in salinity.

TABLE 11.5 Parameters Used to Configure the Hydrology Dynamics for the Three Hypothetical Climate Change Scenarios

Scenario	Precipitation	Evapotranspiration	ESLR (m)	Subsidence
A	>Historical	<Historical	0.43	20%
B	>Historical	Historical	0.63	20%
C	Historical	Historical	0.83	50%

ESLR is eustatic sea level rise, given as the total increase in sea level over the 50-year modeling period. Subsidence is given as a percentage into the range of subsidence rates that occur in different parts of coastal Louisiana (Meselhe et al., 2015).

The extent of future eustatic sea level rise (ESLR) varies among scenarios, where each successive scenario assumes progressively higher ESLR. The scenarios are parameterized in terms of ESLR, soil subsidence, and precipitation. The values for precipitation and evaporation for different scenarios were chosen based on downscaled global climate models (Meselhe et al., 2015). Subsidence rates for Louisiana's coast were based on available data and expert panel input (Meselhe et al., 2015). Rates of ESLR are based on the IPCC predictions adjusted based on Boesch et al. (2013) local adaptive approach (Meselhe et al., 2015). Increases in ESLR and subsidence result in increased coastal inundation. Water depth, duration of flooding events, and spatial extent of flooding are all positively correlated with increases in ESLR and subsidence. The extent to which salt water penetrates into the coastal marshes and swamps is controlled by the sea level variations in the Gulf of Mexico. Increases in rainfall also increase flooding but have the opposite effect on salinity.

Scenario A (Table 11.5) assumes the lowest rate of ESLR and the lowest rate of soil subsidence. Accordingly, this scenario results in the least extensive flooding and the least extensive intrusion of saltwater relative to the other scenarios considered. Scenario B represents a ~50% increase in the rate of ESLR. Scenario C assumes a doubling of ESLR and a 30% increase in subsidence compared to scenario A.

11.2.1.4 Model Results

All three climate change scenarios show similar patterns over the first 20 years of the simulation (Fig. 11.3). During the first 20 years, land area remains remarkably stable, as does the distribution of the estuarine gradient. However, in the first 20 years, the model also predicts some changes within the different salinity zones. In the brackish zone, *D. spicata* expands at the expense of *S. patens*. In the fresh zone *Sagittaria lancifolia* and *P. hemitomon* decline, while *E. baldwinii* and *H. umbellata* increase.

In the last 30 years of the simulation, the effects of climate change become more apparent, with drastic losses of marsh in scenario C, and smaller but significant losses in scenario A. Under all scenarios, land loss occurs (Fig. 11.4) and fresh water marshes are invaded by brackish and saline marshes as the estuarine gradient shifts up the estuaries. Under scenarios A and B, only *D. spicata* and *Paspalum vaginatum* increase their cover, while all other species decline in the last 30 years of the simulation. Under scenario C, the increases of *D. spicata* and *P. vaginatum* start around year 15 and continue for about 10 years, while after year 25 all species decline in cover and only 5% of the model domain remains vegetated.

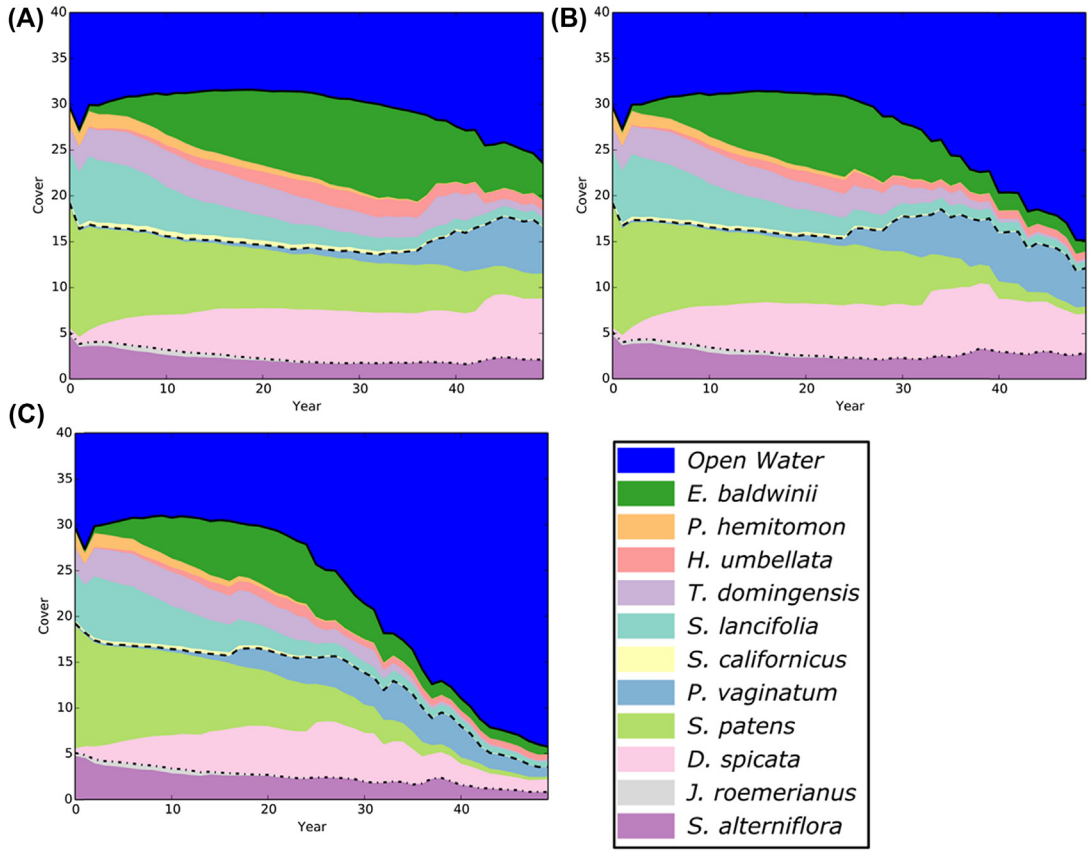

FIGURE 11.3 A summary of simulated regional changes in species composition under scenarios A–C (panels A–C) for 13 of the 19 emergent wetland species with the cover >1% of the model domain at any point during the 50-year simulation period. Species that are not shown had very low cover values. The six most abundant species are freshwater species *Eleocharis baldwinii*, *Hydrocotyle umbellata*, *Morella cerifera*, *Panicum hemitomon*, *Typha domingensis*, and *Sagittaria lancifolia*. The next in abundance are the intermediate salinity species *S. lancifolia* and *Schoenoplectus californicus*, followed by brackish species *Paspalum vaginatum* and *Spartina patens*. Polyhaline marsh species *Distichlis spicata*, *Spartina alterniflora*, *Juncus roemeriaunus*, and *Avicennia germinans* have the lowest abundance.

As apparent sea-level rise increases, the model predicts a shift and shortening of the estuarine gradient upslope (Fig. 11.4). In many areas that are occupied by swamp forest today, the model predicts a change to fresh marsh (Scenario A), brackish marsh (Scenario B), or open water (Scenario C) at the end of the 50-year simulation period. The only region that is relatively stable is the central part of the coast, where the Atchafalaya River maintains coastal freshwater marshes in its delta. In the Atchafalaya River flood plain, bottomland hardwood forest is to a great extend replaced by the more flood tolerant swamp forest species. Along the western part of the coast the areas currently occupied by fresh and brackish marsh species convert to more salt-tolerant species under scenario A, saline marsh species, and open water under scenario B and almost complete conversion to open water under

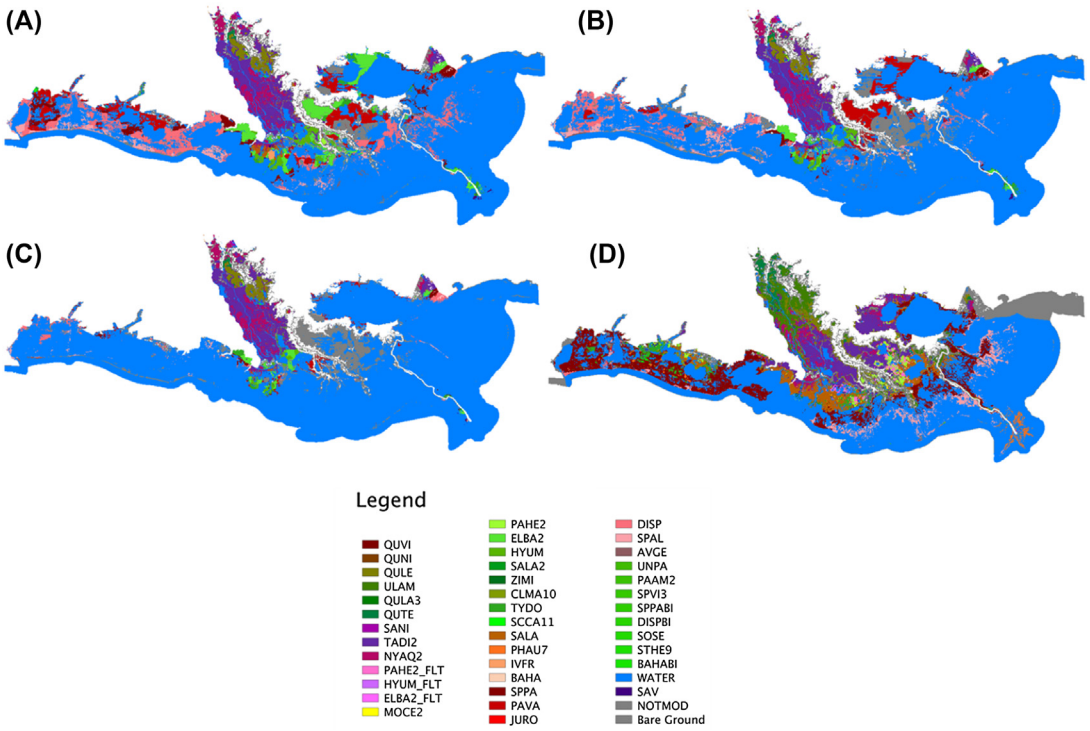

FIGURE 11.4 The forecasted change in species composition in year 50 of the simulation under scenarios A–C (panels A–C) and at the start of the simulation (panel D). Species codes in the legend are provided in Table 11.1.

scenario C. Importantly, these model results suggest that future land loss in the study region could be much faster compared to predictions from previous studies (e.g., Visser et al., 2013). Under the higher ESLR and slightly lower subsidence rates used in this study, the model predicts a near-total loss of the Louisiana coastal wetlands within the next 50 years (Fig. 11.4). This is significantly faster than proposed by Blum and Roberts (2009), who predicted a similar collapse by the year 2100.

11.2.2 Modeling the Impacts of Climate Change on Gulf of Mexico Hypoxia

Hypoxia refers to conditions in the water column where dissolved oxygen falls below levels that can support most marine life (i.e., 2 mg O_2 L^{-1}). The number of coastal hypoxic zones, often referred to as "dead zones," has been increasing at an exponential rate since the 1960s and there are currently over 500 documented coastal hypoxic zones (Diaz and Rosenberg, 2008). Hypoxia causes large-scale spatial population displacement and often mass mortalities of marine organisms that live on or near the bottom (Craig and Crowder, 2005; Breitburg et al., 2009). Hypoxia can also negatively affect the growth and reproduction of commercially important species (Rose et al., 2009).

The northern Gulf of Mexico shelf (NGOM) is the site of one of the world's largest coastal hypoxic zones (up to 22,000 km^2, Rabalais et al., 2007). Hypoxia typically occurs from March

through October in waters below the pycnocline (~10 m) and extends from the depths of ~5 m near the shore to as deep as 60 m at the offshore boundary of the hypoxic zone (Rabalais et al., 2007). Historical reconstruction based on dated sediment cores (Turner and Rabalais, 1994; Osterman et al., 2008; Osterman et al., 2009) and model hindcasts (Justic et al., 2002) indicate that bottom-water hypoxia started to develop in the early part of the twentieth century and has become more frequent and widespread since the 1960s. The temporal increase in the extent and severity of hypoxia has been largely attributed to the increased nitrogen inputs by the Mississippi River and more balanced nutrient ratios in fresh waters (Turner et al., 2012). However, it was also recognized that development of hypoxia in the NGOM is highly sensitive to interannual variability in the Mississippi River discharge. During the drought of 1988 (a 52-year low discharge record of the Mississippi River), for example, the areal extent of midsummer hypoxia was minimal. In contrast, during the flood of 1993 (a 62-year maximum discharge for August and September) the hypoxic zone doubled in size, relative to the 1985–1990 average (Rabalais et al., 2007).

Hypoxia in the NGOM develops as a synergistic product of high surface primary production and high stability of the water column. High surface primary production fuels the water column and benthic respiration by increasing the vertical flux of organic carbon while high stability of the water column inhibits mixing and oxygen resupply to bottom waters. Consequently, climate change could affect the extent and the severity of hypoxia in two major ways. First, changes in temperature and riverine freshwater inputs (Sperna Weiland et al., 2012; IPCC, 2014) would likely modify the spatial and temporal patterns of productivity and respiration. Also, the physical characteristics of the environment (i.e., stratification) would likely change, resulting in more favorable conditions for hypoxia development (Justic et al., 2005).

11.2.2.1 Hypoxia Models

A number of different hypoxia models have been developed for NGOM over the past 20 years, ranging from simple statistical models to complex three-dimensional (3D) coupled hydrodynamic–biogeochemical models (Justic et al., 2007). Recent advances in three-dimensional (3D) coupled hydrodynamic-water quality models for the NGOM hypoxic zone (e.g., Hetland and DiMarco, 2008; Wang and Justic, 2009; Fennel et al., 2013; Justic and Wang, 2014) allow for a more detailed assessment of changes in the spatial patterns of hypoxia in response to climate change.

The effects of climate change on hypoxia in the NGOM have been modeled previously using relatively simple models. For example, Donner and Scavia (2007) examined climate change impacts on hypoxia using a modified Streeter–Phelps model. In a related study, Justic et al. (1996, 2003) used a two-box model to evaluate the impacts of double CO_2 scenario on dissolved oxygen dynamics at a site within the core of the NGOM hypoxic zone. The model assumes uniform properties for the layers above and below the average depth of the pycnocline. The oxygen concentration in the upper water column changes as a result of biological oxygen production and consumption, oxygen transport in the horizontal and vertical direction, and atmospheric exchanges. The oxygen concentration in the lower water column reflects the balance between oxygen uptake due to the benthic and water column respiration and oxygen resupply from the upper water column via turbulent diffusion (Justic et al., 2002). Model scenarios included a historical baseline conditions for the period 1955–2000 and six hypothetical future scenarios that were based on observed and projected changes

in the Mississippi River discharge, Mississippi River nitrate concentrations, and ambient water temperatures (Justic et al., 2003).

Here, the predictions of the Justic et al. (2003) model are supplemented by the new results from the high resolution, coupled hydrodynamic-biogeochemical FVCOM-WASP model (Justic and Wang, 2014). FVCOM is a 3D, primitive equation coastal ocean circulation model that features an unstructured triangular grid to resolve complex coastlines and a terrain following coordinate system to convert irregular bottom topography into a regular computational domain (Chen et al., 2003). The current implementation for the NGOM uses 14,740 triangular nodes and 28,320 triangular elements, and has a variable 1–10 km horizontal resolution. The vertical grid domain consisted of 31 uniformly distributed σ layers. The WASP water quality model simulates nitrogen and phosphorous kinetics, carbonaceous biological oxygen demand in the water column and sediments, phytoplankton biomass (expressed as carbon and chlorophyll), and dissolved oxygen dynamics (Justic and Wang, 2014).

11.2.2.2 Model Results

Box-model run for historical baseline conditions (1955–2000) predicted the occurrence of hypoxia in 19 out of 45 simulated years, 16 of which were years with severe hypoxia when the dissolved oxygen concentrations decreased below 1 mg/L (Fig. 11.5). The model results also suggested that hypoxia first appeared in the mid-1970s and has become more severe over time. The predicted onset of hypoxia is in good agreement with the timing of first reports documenting hypoxia in this region (Rabalais and Turner, 2001) and the incidence of hypoxia proxies in dated sediment cores from the hypoxia region (e.g., Turner and Rabalais, 1994). For a future hypothetical climate scenarios characterized by 4°C temperature increase and a 20% increase in the average annual Mississippi River discharge (Justic et al., 2003), the model predicted 31 years with hypoxia, 26 of which were years with severe hypoxia (Fig. 11.5).

The FVCOM-WASP model simulations for 2002 showed a good agreement between simulated and observed areal extent of hypoxia (Fig. 11.6). The simulated area of hypoxia during July 2002 was 18,550 km^2, which was about 15% lower than the area of hypoxia measured during the concurrent hypoxia monitoring cruise (22,000 km^2, www.gulfhypoxia.net). The measured area of hypoxia during July 2002 was the highest since the monitoring program started in 1985 (Rabalais et al., 2007) and provides a good reference for the baseline model scenario. Assuming a 4°C increase in temperature and a 20% increase in the average annual Mississippi River discharge, the FVCOM-WASP model predicts an approximate doubling in the area of hypoxia compared to the baseline model scenario, along with severely reduced bottom oxygen levels over much of the study area and expansion of hypoxia into deeper waters on the continental shelf (Fig. 11.6).

11.2.3 Modeling the Impacts of Climate Change on Coastal Ecosystems in the Western Pacific

The Western Pacific is a vast marginal ocean stretching from 6°N to 42°N and consisting of several marginal seas including the Bohai Sea, Yellow Sea, East China Sea, and South China Sea. The circulation in these marginal seas is controlled by a strong M2 tide and two monsoon systems, the East Asian Monsoon from the east and the Indian Monsoon from the south. Meanwhile, the Western Pacific receives discharges from several large river systems,

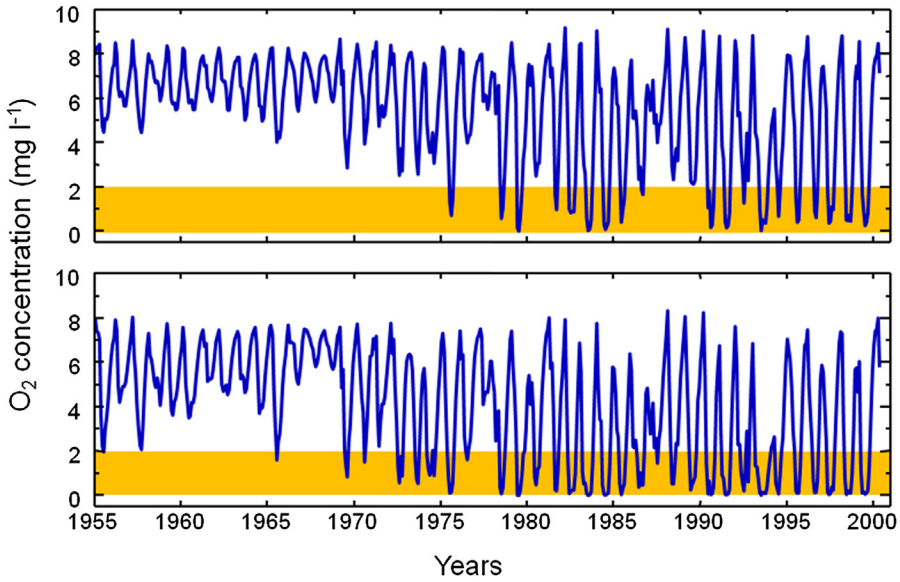

FIGURE 11.5 Simulated changes in the average bottom oxygen concentrations at a station within the core of the northern Gulf of Mexico hypoxic zone for the 1955–2000 baseline scenario (top panel), and for a hypothetical future scenario that assumes a 4°C increase in temperature and a 20% increase in the Mississippi River discharge (bottom panel). Shaded areas denote hypoxic conditions (<2 mg O_2 L^{-1}). *Adapted from Justic, D., Rabalais, N.N., Turner, R.E., 2003. Simulated responses of the Gulf of Mexico hypoxia to variations in climate and anthropogenic nutrient loading. Journal of Marine Systems 42, 115–126.*

including the Yellow River (Huanghe), Yangtze River (Changjiang), Pearl River (Zhujiang), Red River (Songhong), and Mekong River (Lancang), all of which originate from the Qinghai-Tibetan Plateau. These large rivers travel thousands of kilometers before entering the ocean and deliver large amounts of sediments along with nutrients and other particulate and dissolved constituents. Annual and decadal changes in the constituent fluxes of these large rivers reflect the climatic and anthropogenic influences in their massive watersheds and provide an excellent research framework to examine the potential consequences of future climate change.

The marginal seas in the Western Pacific are also bordered by some of the most densely populated coastal regions in the world. Human activities, mainly through dam construction and deforestation, have dramatically reduced sediment delivery to the coastal ocean. The total annual sediment flux from these rivers has decreased from 20 to 6 million tons per year over the past century (Wang et al., 2011), which when combined with the rising sea level, seriously threatens the sustainability of the coastal communities. On these heavily populated deltaic coasts, the blooming economic activities are further contributing to land subsidence via ground water extraction, various coastal engineering projects, and changes in land use practices. The Mekong Delta, for example, was listed as the most endangered delta in the world by the Intergovernmental Panel on Climate Change (IPCC, 2007).

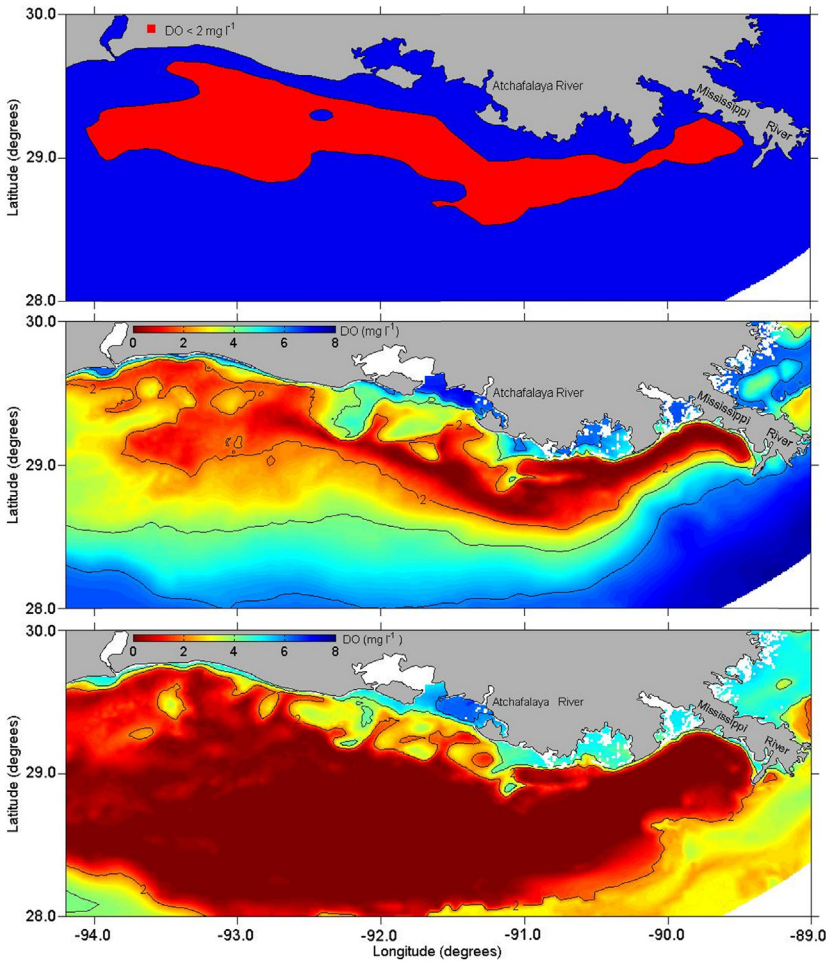

FIGURE 11.6 Measured area of bottom water hypoxia (<2 mg O_2 L^{-1}) in the northern Gulf of Mexico during July 21–26, 2002 (top panel, www.gulfhypoxia.net). Also shown are the simulated bottom oxygen concentrations during July 21–26, 2002, for the baseline scenario (middle panel, adapted from Justic and Wang, 2014), and for a hypothetical future scenario that assumes a 4°C increase in temperature and a 20% increase in the Mississippi River discharge (lower panel). The area of hypoxia is denoted by the 2 mg O_2 L^{-1} isoline.

11.2.3.1 Monsoon Dynamics

Climate in the Western Pacific is dominated by the East Asian Monsoon and South Asian Monsoon (Indian Monsoon). Monsoons impact to the Western Pacific region in various ways. In the ocean, monsoons are affecting the circulation and the associated biogeochemical processes via wind, pressure, heat, and freshwater flux. On land, monsoons are controlling the snow formation and melting on the Tibetan Plateau, and so they affect riverine discharge and constituent transport to the coastal ocean. Potential impacts of climate change on monsoon dynamics were explored using various global coupled ocean–atmosphere general

circulation models (e.g., Kripalani et al., 2006; Kripalani et al., 2007; Turner and Annamalai, 2012). Results from a multimodel ensemble projected a significant increase in summertime precipitation under future climate scenarios for both the East Asian (7.8%) and the Indian Monsoons (8.0%). The dynamics of the East Asian Monsoon is more complex compared to the Indian Monsoon due to its subtropical origin and close coupling to ENSO (Wang et al., 2000). For the Indian monsoon, the model results point to a longer monsoon season (June–September) and more variable precipitation pattern, in response to intensified heat flow over northwest India (Kripalani et al., 2007).

While most of existing modeling studies were focused on changes in the precipitation pattern, potential changes in the wind forcing would also have important implications for the coastal ecosystems in the Western Pacific. The pattern of coastal surface winds during winter monsoon controls the resuspension and alongshore transport of river-derived materials (e.g., Xue et al., 2012). Coastal circulation in the vicinity of large river deltas along the Western Pacific margin is largely dominated by the geostrophic balanced currents, which will be enhanced by the downwelling favorable northeasterly winds. The results from a multimodel ensemble predict an increase in wind speed in the global monsoon regions and a reduction in wind speed over most of the tropical oceans (Hsu et al., 2013). For instance, the northwesterly winds along the coastal region of north Western Pacific would increase significantly in response to global warming (Xu et al., 2015).

11.2.3.2 Sediment Transport

Over the past 9000 years, the five large river deltas (Yellow, Yangtze, Pearl, Red, and Mekong) have been prograding toward the Western Pacific because of the annual supply of millions of tons of sediments together with a relative steady sea level. However, this process will likely be reversed under projected future climate scenarios due to rising sea level. For instance, by the end of this century, sea-level rise in the South China Sea is projected to increase by 0.64 m (Huang and Qiao, 2015).

With advances of high performance computing and algorithm development, sediment transport models have become an important tool in assessing the potential impacts of climate change on continental shelf processes. These sediment models are generally used in conjunction with ocean circulation models, such as the Regional Ocean Modeling System (ROMS, e.g., Shchepetkin and McWilliams, 2005; Haidvogel et al., 2008), and allow for characterization of bottom boundary layers and description of cohesive sediment behavior. One notable development was the Coupled Ocean Atmosphere Wave and Sediment Transport modeling system (COAWST, Warner et al., 2010). The COAWST couples sediment transport with wave and atmospheric forcings and includes the ROMS, the Weather Research Forecast model (WRF, Skamarock et al., 2005), and the Simulate WAve Nearshore model (SWAN, Booij et al., 1999). This coupled modeling system allows for efficient exchange of information (air pressure, heat flux, sea surface temperature, sea level, etc.) among different models. Also, the close coupling between waves and ocean circulation allows the estimation of wave-induced enhancement of surface roughness, water column mixing, and bottom stress, all of which are critical for sediment transport modeling.

Recently the COAWST was applied to the Western Pacific to simulate the sediment transport and deposition on the continental shelf. In one of the COAWST applications Xue et al. (2012) simulated coupled ocean, wave, and sediment transport dynamics. The model

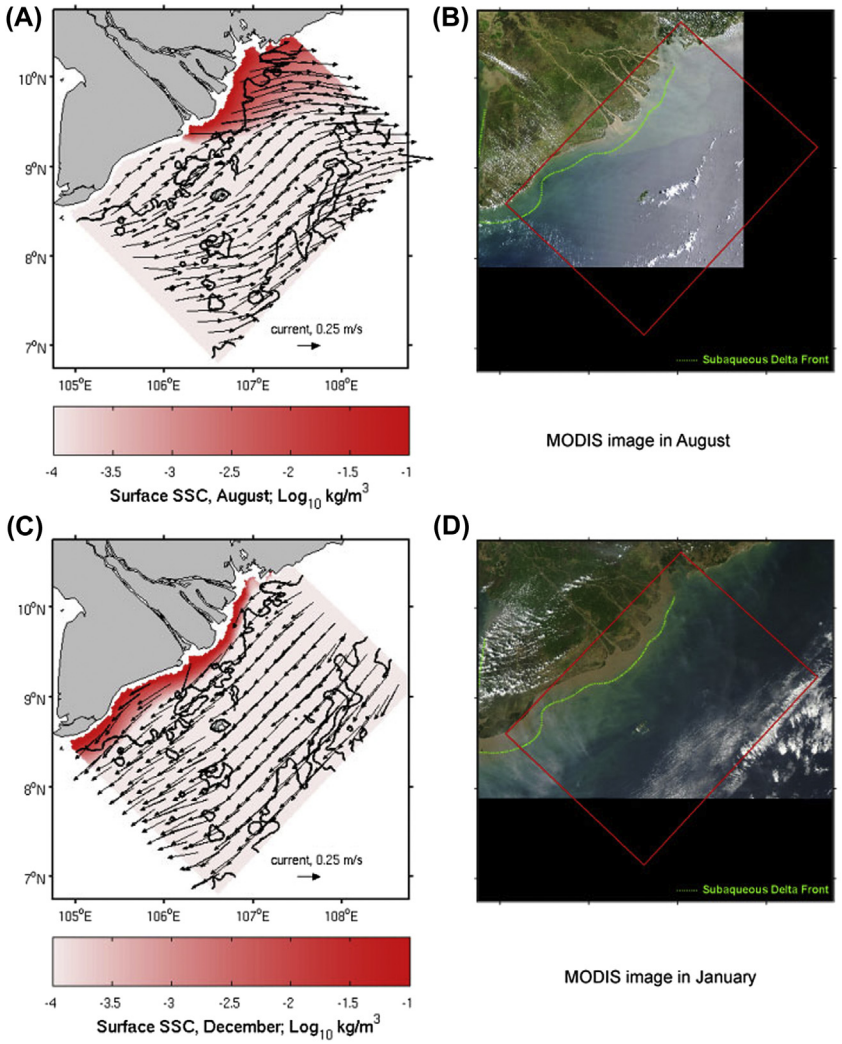

FIGURE 11.7 Monthly mean surface suspended sediment concentration (SSC, color shading) and surface current fields in (A) summer (August) and (C) winter (December), 2005. Also shown are Moderate Resolution Imaging Spectroradiometer (MODIS) images in August 2002 (B) and January 2005 (D). Simulated surface SSC values (kg/m^3) are shown on the log scale (color). *From Xue, Z., He, R., Liu, J.P., Warner, J.C., 2012. Modeling transport and deposition of the Mekong River sediment. Continental Shelf Research 37, 66–78; reprinted with permission from Elsevier.*

accurately described the seasonal shift of monsoonal winds and associated sediment transport on the Mekong Shelf and confirmed the previously proposed "summer deposit–winter transport" mechanism for large river-derived sediments in the Western Pacific (Fig. 11.7). Using the COAWST, Bian et al. (2013) examined the transport pathways of shelf sediments in the Bohai-Yellow-East China Seas under climatological mean circulation and wind forcing.

Further, the modeling results suggested that most of the sediments supplied by the Yellow River remain within the Bohai Sea, whereas the Yangtze-derived sediments are transported to the Yellow and East China Seas (Zeng et al., 2015).

While the current state-of-the-art sediment transport models show reasonable skill in quantifying sediment fluxes and reproducing the patterns of sediment distribution, much remains to be learned regarding the response of sediment transport to combined effects of sea-level rise and changes in monsoonal regime. Further, ongoing human activities in river basins and along the coast make the forecasting of future conditions even more challenging (Syvitski et al., 2009). For instance, projected increases of summer monsoon precipitation will likely intensify inland erosion and thus increase riverine-suspended sediment load. However, because a large fraction of suspended sediment load is deposited behind dams, it remains unclear whether the altered monsoon dynamics would significantly affect the overall sediment delivery to the Western Pacific.

11.2.3.3 Coastal Ecosystem Processes

Ecosystems of the Western Pacific marginal seas are highly sensitive to climate-driven variability in monsoon dynamics and changes in sediment and nutrient fluxes at land-ocean interface (e.g., Liu et al., 2014). For example, model estimates by Liu et al. (2010) suggest that primary productivity in the East China Sea increased by 17% between 1970 and 2002. This increase in primary productivity was caused by a 2.4-fold increase in the dissolved inorganic nitrogen load of the Yangtze River over the same period of time (Liu et al., 2015). While in the coastal regions primary productivity is predominantly controlled by the riverine nutrient inputs, in the open ocean it is sustained largely by the nutrients supplied by the monsoon-induced upwelling. A coupled physical–biological model developed by Liu et al. (2002) successfully simulated the existence of three distinct high-chlorophyll regions in the South China Sea, which correspond to the monsoon-influenced upwelling regions that develop northwest of Luzon and north of the Sunda Shelf in winter and off the east coast of Vietnam in summer. Chai et al. (2009) used the ROMS CoSINE ecosystem model to examine the carbon budget of the Western Pacific. They concluded the South China Sea is overall a weak source CO_2 for the atmosphere.

In a related study, Glibert et al. (2014) used the Global Coastal Ocean Modelling System (GCOMS, Holt et al., 2009) to examine the changes in harmful algal bloom distribution in response to climate change. The model was forced by atmospheric and oceanic boundary conditions from the IPCC climate models and river inputs were derived from the NEWS model (Global Nutrient Export from Watersheds, Seitzinger et al., 2005). Projections from this coupled model suggested that HAB potential in the Yellow and East China seas will not change substantially by the end of this century. However, it should be pointed out that our understanding of the linkages between climate variability and HABs in this region is still very limited.

11.2.4 Modeling the Impacts of Climate Change on the California Current System

Four major coastal upwelling systems, including the California upwelling system, the Humboldt upwelling system, the Canary upwelling system, and the Benguela upwelling

system, account for less than 2% of the ocean, yet support more than 20% of the global fish catch (Pauly and Christensen, 1995). Located at the eastern boundaries of the four subtropical gyres in both the Pacific and the Atlantic oceans, coastal upwelling systems are driven by seasonal equatorward winds that push surface water offshore and subsequently bring subsurface water closer to the coast. The subsurface water is distinctly different from surface water in its physical and chemical properties. It is low in temperature, enriched in nutrients, deficient in dissolved oxygen and enriched in dissolved inorganic carbon (DIC). The upwelled nutrients fuel the surface ocean productivity, while the shallow hypoxia depth and aragonite saturation depth limit the vertical distribution of marine organisms. The abundance of DIC in upwelled water also makes the region a source of atmospheric CO_2.

11.2.4.1 Modeling of the California Current System

Observational programs in the California Current system (CCS), most notably the California Cooperative Oceanic Fisheries Investigations (CalCOFI) time series that started at 1949 (Bograd et al., 2003), have significantly advanced our understanding of the physics, chemistry, ecology, and fisheries in the CCS. Early ecosystem modeling studies relied on physical models of reduced complexity, such as one-dimensional (e.g., Moisan and Hofmann, 1996) and two-dimensional models (e.g., Spitz et al., 2003). Ecosystem in CCS is highly modulated by three-dimensional circulation; however, those simplified physical models provided a useful basis for the development of ecological models of the CCS. Subsequently, Gruber et al. (2006) embedded a nitrogen-based Nutrient-Phytoplankton-Zooplankton-Detritus (NPZD) model within the 3D Regional Oceanic Modeling System (ROMS) and ran the coupled model for 10 years so that a climatological equilibrium was reached. The NPZD model simulates the dynamics of two macronutrients (nitrate and ammonia), one phytoplankton group (i.e., diatoms), chlorophyll-to-carbon ratio of phytoplankton, one zooplankton group, and two detritus pools with different sinking speeds. By a comprehensive comparison with different satellite products and in situ measurements, the authors showed that this relatively simple ecological model was able to skillfully reproduce the spatial and temporal distributions of temperature, nutrients, and chlorophyll in the CCS.

Superimposed on the large-scale equatorward eastern boundary currents and the upwelling flows are mesoscale eddies arising from the unstable sheared currents and tilting thermocline. Mesoscale activities are important source of nutrients in the open ocean, particularly in oligotrophic ocean gyres (McGillicuddy et al., 1998; Levy et al., 2001). Cyclonic eddies uplift thermocline/nutricline during their passage and pump nutrients from subsurface into the eutrophic zone. In the eastern boundary upwelling systems, however, eddy activities are negatively correlated with upper ocean productivity (Gruber et al., 2011). By contrasting models that resolve eddies with models that do not, Gruber et al. (2011) showed that mesoscale eddies bury upwelled nutrients during their offshore propagation. Since thermocline shoals toward the coast and material transport by eddies is largely along isopycnals, there is a downward component in material transport by westward offshore eddy propagation. The reduction in nearshore production also leads to lower nutrient content in source water for upwelling by reducing the amount of sinking organic matters. Subsequent studies (e.g., Combes et al., 2013; Nagai et al., 2015) further demonstrated that anticyclonic eddies have a larger contribution for offshore downward material transport than cyclonic eddies. Using a Lagrangian particle tracking module in the 3D

circulation model, Lachkar and Gruber (2011) showed that strong eddy activity contributes to relatively low nutrient residence time and nutrient utilization rate in the CCS compared to the Canary current system.

11.2.4.2 Future Evolution of the California Current System

Due to its prime importance in climate, environment, and fishery, the future evolution of coastal upwelling systems has received considerable attention. Bakun (1990) proposed a mechanism demonstrating that the equatorward upwelling-favorable winds strengthen under rising atmospheric CO_2 concentrations. The equatorward upwelling-favorable wind is a geostrophic wind driven by large-scale land-sea pressure difference. Each spring and summer when the hemisphere warms up, the land warms up faster than the ocean because of its smaller heat capacity, and a low-pressure cell develops above the land. With the build-up of CO_2 and other greenhouse gases in the atmosphere, more heat is trapped and further enhances the land−ocean temperature and pressure gradients, leading to stronger geostrophic upwelling favorable winds. The intensification of upwelling favorable winds has been observed in both historical wind measurements (e.g., Sydeman et al., 2014) and in simulated future climate scenarios (Wang et al., 2015).

The ecological consequences of the wind strengthening embedded in a warming, souring, and deoxygenating ocean, is less certain. Biological production increases as a result of upwelling intensification that enhances nutrient supply to the euphotic zone. The increase in biological production, however, is not proportional to the increase in wind stress. Lachkar and Gruber (2013) showed that a doubling of wind stress results in less than 50% increase in biological production in the California current system while the same increase in wind stress doubles production in the Canary current system. The relatively low increase in the productivity of the California current system is a combined result of low phytoplankton growth under nutrient replete conditions and strong offshore transport. The authors also looked at influence of doubling wind stress on air−sea CO_2 flux (with a constant atmospheric CO_2 concentration). They showed that the doubling of wind stress increases air−sea CO_2 efflux by 4−6 times in central California and southern Canary current and yet has little effect on other upwelling regions. The doubling of wind stress not only increases the upwelled supply of DIC and biological consumption but also enhances the wind-dependent gas transfer rate. Regional differences in the relative importance of the DIC supply, biological consumption, and gas transfer lead to the differences in the variability of CO_2 flux.

The California current system is a hotspot of ocean acidification which has a negative impact on calcifying marine organisms and aquaculture (e.g., Barton et al., 2012). Coastal water in the CCS (and in other eastern boundary upwelling systems) is naturally more acidic than other oceanic regions because upwelling brings DIC-enriched and carbonate-depleted deeper water to the surface. The large subsurface remineralization of sinking organic matter further makes the source water for upwelling even more acidic. Feely et al. (2008) observed seawater with pH values as low as 7.75, and aragonite undersaturation starting at depths varying from the 120 m to the surface in the northern US pacific coast. Hauri et al. (2009) reproduced the observed pattern of pH and aragonite undersaturation with an NPZD model coupled with an equilibrium carbon chemistry module embedded in ROMS. Using climatological forcing conditions except a rising atmospheric CO_2 concentration, Gruber et al. (2012)

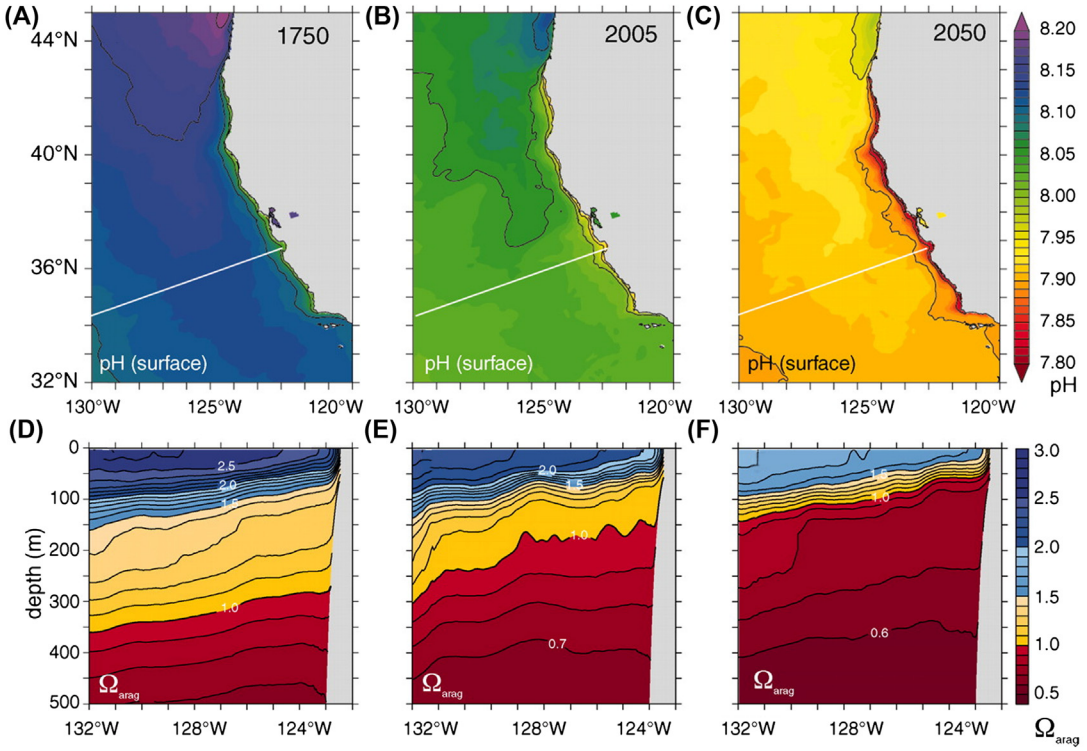

FIGURE 11.8 Temporal evolution of ocean acidification in the California Current system from 1750 until 2050. Maps A to C show the modeled pH values for 1750, 2005, and 2050. Maps D to F illustrate decrease in the annual mean saturation state of seawater with respect to aragonite (Ω_{arag}) and the shoaling of the aragonite saturation depth ($\Omega_{arag} = 1$). The white lines in panels A to C indicate the position of the offshore transect. *From Gruber, N., Hauri, C., Lachkar, Z., Loher, D., Frolicher, T.L., Plattner, G.K., 2012. Rapid progression of ocean acidification in the California Current system. Science 337, 220–223; reprinted with permission from AAAS.*

and Hauri et al. (2013a,b) projected that more than half of the water in eutrophic zone would be undersaturated with respect to aragonite by the year 2050 and bottom water would become year-round undersaturated within the next 20–30 years (Fig. 11.8). Lachkar (2014) included the upwelling intensification in the acidification projection simulations and showed that upwelling intensification strengthens acidification in the California current and weakens acidification in the Canary current. In the California current, stronger upwelling of acidic water dominates while in the Canary current, reduced remineralization due to strengthening of offshore organic matter transport and increased biological production appears more important.

Hypoxia occurs in the CCS during summer upwelling seasons. Unlike other coastal systems where nutrient loading from human activities play a significant role (e.g., Rabalais et al., 2009, 2010), hypoxia in the CCS and other upwelling systems is primarily controlled by upwelling intensity and oxygen contents in upwelled source water (Grantham et al., 2004). Observations have shown the decline in oxygen content in southern California waters

from 1984 to 2006 (Bograd et al., 2008). Using an NPZD model coupled with ROMS, Lachkar and Gruber (2012) showed that wind intensification increases the amount of hypoxic water in the California current system while decreases the amount of hypoxic water in the Canary current system. Similar to the above-illustrated mechanisms controlling the variability in ocean acidification, increase in advection of oxygen-poor water controls the volume of hypoxic water in the California current. In contrast, the increase in biological oxygen production lessens hypoxia in the Canary current.

In addition to changes in the upwelling regime, variability in large-scale circulation associated with global warming also play significant role in the CCS by modulating the properties of the upwelled source water. By analyzing solutions from NOAA's coupled biogeochemical–physical general circulation model, Rykaczewski and Dunne (2010) suggested that source waters for the upwelling could be more enriched in nitrate and more depleted in oxygen under future climate conditions. This is because surface water warms up faster than deep water, resulting in stronger stratification. Consequently, the ventilation of deep water capped by a stronger thermocline slows down, resulting in stronger remineralization, nutrient accrual, and oxygen depletion.

11.3 CHALLENGES IN PREDICTING THE EFFECTS OF CLIMATE CHANGE ON COASTAL ECOSYSTEMS

The four case studies presented above illustrate the power of simulation modeling in projecting future conditions in the coastal zone and the wealth of information and details they can provide. However, while significant advances in numerical modeling have been made, there are also continuing challenges in modeling the effects of climate change on coastal ecosystems (e.g., Rose and Allen, 2013). For example, most global climate models (e.g., IPCC/CMIP5) have a relative coarse resolution ($\sim 1^{\circ}$) and do not account for many coastal processes such as inundation, estuarine-shelf exchanges, and riverine freshwater, sediment, and nutrient inputs. Further, wind drop-off toward the coast, coastal upwelling, and formation of eddies are all poorly resolved in global models, which decreases the accuracy of ocean–atmosphere momentum and heat flux estimates. Also, using products from global models to drive regional models is not trivial and the computational expense of dynamically downscaling a 100-year global atmospheric forcing to a regional scale remains formidable obstacle for many researchers working in coastal ecosystems. Statistical downscaling, while computationally much less intensive, largely depends on the existing predictor–predictand relationship and cannot incorporate future climatic changes. The existing regional ecosystem models also need improvement. For example, there are still large uncertainties in the numerical formulations of biogeochemical and food web processes. Model formulations are often semiempirical with parameters tuned to best match historical observations. It is uncertain how reliable those models can be for future conditions that will likely include different environmental conditions and altered coastal food webs. Finally, as model spatial and temporal domains increase due to developments in computer technologies and computational techniques, much work remains to be done to enhance data collection in support of model calibration and validation.

11.4 CONCLUSIONS

Numerical simulation models play important roles in assessing the potential effects of climate change on coastal ecosystems and developing management strategies aimed at minimizing risks to sensitive habitats, species, and people living along the coasts. Numerical models also provide a quantitative framework to disentangle the synergistic influences of multiple factors and isolate the effects of individual stressors. This is important because climatic drivers do not act alone, but rather in conjunction with other ecosystem stressors, such as habitat degradation, pollution, eutrophication, and overharvesting of commercially important species. Undoubtedly, coastal ecosystem models will continue to evolve and will play even larger roles as computational power increases and time-series of observed climatic and environmental variables become longer and more informative. There is every reason to be optimistic that continued model improvement will lead to better understanding of coastal ecosystems, more instructive climate impact assessments, and better informed management decisions.

Acknowledgments

Hypoxia modeling effort carried out by D. Justic was funded in part by the NOAA/CSCOR Northern Gulf of Mexico Ecosystems and Hypoxia Assessment Program under award NA09NOS4780230 to Louisiana State University. Drs. Duke-Sylvester and Visser, who contributed the section on modeling the effects of climate change on Louisiana's coastal wetland plant communities, were supported by the Louisiana Coastal Protection and Restoration Authority through The Water Institute of the Gulf under project award number CPRA-2013-T03-EM, as part of a larger effort to support of the development of Louisiana's 2017 Coastal Master Plan. The views expressed in this publication are those of the authors and do not necessarily represent the views of the Coastal Protection and Restoration Authority or The Water Institute of the Gulf.

References

Bakun, A., 1990. Global climate change and intensification of coastal ocean upwelling. Science 247, 198–201.

Baldwin, A.H., Batzer, D.P., 2012. Wetland Habitats of North America: Ecology and Conservation Concerns. University of California Press, Oakland, California.

Barton, A., Hales, B., Waldbusser, G.G., Langdon, C., Feely, R.A., 2012. The Pacific oyster, Crassotrea gigas, shows negative correlation to naturally elevated carbon dioxide levels: implications for near-term ocean acidification effects. Limnology and Oceanography 57, 698–710.

Bendtsen, J., Hansen, J.L.S., 2013. Effects of global warming on hypoxia in the Baltic Sea–North Sea transition zone. Ecological Modelling 264, 17–26.

Bian, C., Jiang, W., Greatbatch, R.J., 2013. An exploratory model study of sediment transport sources and deposits in the Bohai Sea, Yellow Sea, and East China Sea. Journal of Geophysical Research: Oceans 118, 5908–5923.

Blum, M.D., Roberts, H.H., 2009. Drowning of the Mississippi Delta due to insufficient sediment supply and global sea-level rise. Nature Geoscience 2 (7), 488–491.

Boesch, D.F., Atkinson, L.P., Boicourt, W.C., Boon, J.D., Cahoon, D.R., Dalrymple, R.A., Ezer, T., Sommerfield, C.K., 2013. Updating Maryland's SLR Projections. Special Report of the Scientific and Technical Working Group to the Maryland Climate Change Commission. University of Maryland Center for Environmental Science, Cambridge, Maryland.

Bograd, S.J., Checkley, D.A., Wooster, W.S., 2003. CalCOFI: a half century of physical, chemical, and biological research in the California current system. Deep-Sea Research 50 (14–16), 2355–2370.

Bograd, S.J., Castro, C.G., Di Lorenzo, E., Palacios, D.M., Bailey, H., Gilly, W., Chavez, F.P., 2008. Oxygen declines and the shoaling of the hypoxic boundary in the California Current. Geophysical Research Letters 35, L12607.

Booij, N., Ris, R., Holthuijsen, L.H., 1999. A third-generation wave model for coastal regions: 1. Model description and validation. Journal of Geophysical Research: Oceans 104, 7649–7666.

Breitburg, D.L., Hondorp, D.W., Davias, L.A., Diaz, R.J., 2009. Hypoxia, nitrogen, and fisheries: integrating effects across local and global landscapes. Annual Review of Marine Science 1, 329–349.

Chai, F., Liu, G., Xue, H., Shi, L., Chao, Y., Tseng, C.-M., et al., 2009. Seasonal and interannual variability of carbon cycle in South China Sea: a three-dimensional physical-biogeochemical modeling study. Journal of Oceanography 65, 703–720.

Chen, C., Liu, H., Beardsley, R.C., 2003. An unstructured grid, finite-volume, three-dimensional, primitive equations ocean model: application to coastal ocean and estuaries. Journal of Atmospheric and Oceanic Technology 20, 159–186.

Combes, V., Chenillat, F., Di Lorenzo, E., Riviere, P., Ohman, M.D., Bograd, S.J., 2013. Cross-shore transport variability in the California Current: Ekman upwelling vs. eddy dynamics. Progress in Oceanography 109, 78–89.

Craft, C., Clough, J., Ehman, J., Joye, S., Park, R., Pennings, S., Guo, H., Machmuller, M., 2009. Forecasting the effects of accelerated sea-level rise on tidal marsh ecosystem services. Frontiers in the Ecology and Environment 7, 73–78.

Craig, J.K., Crowder, L.B., 2005. Hypoxia-induced habitat shifts and energetic consequences in Atlantic croaker and brown shrimp on the Gulf of Mexico shelf. Marine Ecology Progress Series 294, 79–94.

Davis, S., Ogden, J.C., 1994. Everglades: The Ecosystem and Its Restoration. CRC Press, Boca Raton, Florida.

DeAngelis, D.L., Gross, L.J., Huston, M.A., Wolff, W.F., Fleming, D.M., Comiskey, E.J., Sylvester, S.M., 1998. Landscape modeling for Everglades ecosystem restoration. Ecosystems 1 (1), 64–75.

Denslow, J.S., Battaglia, L.L., 2002. Stand composition and structure across a changing hydrologic gradient: Jean Lafitte National Park, Louisiana, USA. Wetlands 22 (4), 738–752.

Diamond, S., Murphy, C.A., Rose, K.A., 2013. Simulating the effects of global climate change on Atlantic croaker population dynamics in the mid-Atlantic Region. Ecological Modelling 264, 98–114.

Diaz, R.J., Rosenberg, R., 2008. Spreading dead zones and consequences for marine ecosystems. Science 321, 926–928.

Donner, S.D., Scavia, D., 2007. How climate controls the flux of nitrogen by the Mississippi River and the development of hypoxia in the Gulf of Mexico. Limnology and Oceanography 52, 856–861.

Feely, R.A., Sabine, C.L., Hernandez-Ayon, J.M., Ianson, D., Hales, B., 2008. Evidence for upwelling of corrosive "acidified" water onto the continental shelf. Science 320, 1490–1492.

Fennel, K., Hu, J., Laurent, A., Marta-Almeida, M., Hetland, R., 2013. Sensitivity of hypoxia predictions for the Northern Gulf of Mexico to sediment oxygen consumption and model nesting. Journal of Geophysical Research: Oceans 118, 990–1002.

Folse, T.M., West, J.L., Hymel, M.K., Troutman, J.P., Sharp, L.A., Weifenbach, D., McGinnis, T., Rodrigue, L.B., Boshart, W.M., Richardi, D.C., Miller, C.M., Wood, W.B., 2012. A Standard Operating Procedures Manual for the Coast-wide Reference Monitoring System-wetlands: Methods for Site Establishment, Data Collection, and Quality Assurance/Quality Control. Louisiana Coastal Protection and Restoration Authority, Office of Coastal Protection and Restoration, Baton Rouge, Louisiana.

Glibert, P.M., Allen, J.I., Artioli, Y., Beusen, A., Bouwman, L., Harle, J., et al., 2014. Vulnerability of coastal ecosystems to changes in harmful algal bloom distribution in response to climate change: projections based on model analysis. Global Change Biology 20, 3845–3858.

Gochis, D.J., Yu, W., Yates, D.N., 2014. The NCAR WRF-Hydro Technical Description and User's Guide v2.0. http://www.ral.ucar.edu/projects/wrf_hydro/.

Grantham, B.A., Chan, F., Nielsen, K.J., Fox, D.S., Barth, J.A., Huyer, A., Lubchenco, J., Menge, B.A., 2004. Upwelling-driven nearshore hypoxia signals ecosystem and oceanographic changes in the northeast Pacific. Nature 429, 749–754.

Gruber, N., Frenzel, H., Doney, S.C., Marchesiello, P., McWilliams, J.C., Moisan, J.R., Oram, J.J., Plattner, G.K., Stolzenbach, K.D., 2006. Eddy-resolving simulation of plankton ecosystem dynamics in the California current system. Deep-Sea Research 53, 1483–1516.

Gruber, N., Lachkar, Z., Frenzel, H., Marchesiello, P., Munnich, M., McWilliams, J.C., Nagai, T., Plattner, G.K., 2011. Eddy-induced reduction of biological production in eastern boundary upwelling systems. Nature Geosciences 4, 787–792.

Gruber, N., Hauri, C., Lachkar, Z., Loher, D., Frolicher, T.L., Plattner, G.K., 2012. Rapid progression of ocean acidification in the California current system. Science 337, 220–223.

Haidvogel, D.B., Arango, H., Budgell, W.P., Cornuelle, B.D., Curchitser, E., Di Lorenzo, E., et al., 2008. Ocean forecasting in terrain-following coordinates: formulation and skill assessment of the regional ocean modeling system. Journal of Computational Physics 227, 3595–3624.

Hare, J.A., Alexander, M.A., Fogarty, M.J., Williams, E.H., Scott, J.D., 2010. Forecasting the dynamics of a coastal fishery species using a coupled climate-population model. Ecological Applications 20, 452–464.

Hauri, C., Gruber, N., Plattner, G.K., Alin, S., Feely, R.A., Hales, B., Wheeler, P.A., 2009. Ocean acidification in the California current system. Oceanography 22, 60–71.

Hauri, C., Gruber, N., McDonnell, A.M.P., Vogt, M., 2013a. The intensity, duration, and severity of low aragonite saturation state events on the California continental shelf. Geophysical Research Letters 40, 3,424–3,428.

Hauri, C., Gruber, N., Vogt, M., Doney, S.C., Feely, R.A., Lachkar, Z., Leinweber, A., McDonnell, A.M.P., Munnich, M., Plattner, G.K., 2013b. Spatiotemporal variability and long-term trends of ocean acidification in the California current system. Biogeosciences 10 (1), 193–216.

Hetland, R.D., DiMarco, S.F., 2008. How does the character of oxygen demand control the structure of hypoxia on the Texas-Louisiana continental shelf? Journal of Marine Systems 70 (1–2), 49–62.

Holt, J., Harle, J., Proctor, R., Michel, S., Ashworth, M., Batstone, C., et al., 2009. Modelling the global coastal ocean. Philosophical Transactions of the Royal Society of London A: Mathematical, Physical and Engineering Sciences 367, 939–951.

Hsu, P.-C., Li, T., Murakami, H., Kitoh, A., 2013. Future change of the global monsoon revealed from 19 CMIP5 models. Journal of Geophysical Research: Atmospheres 118, 1247–1260.

Huang, C., Qiao, F., 2015. Sea level rise projection in the South China Sea from CMIP5 models. Acta Oceanologica Sinica 34, 31–41.

IPCC, 2007. In: Parry, M.L., Canziani, O.F., Palutikof, J.P., Van Der Linden, P.J., Hanson, C.E. (Eds.), Contribution of Working Group II to the Fourth Assessment Report of the Intergovernmental Panel on Climate Change. Cambridge University Press, Cambridge & New York.

IPCC, 2014. In: Barros, V.R., Field, C.B., Dokken, D.J., Mastrandrea, M.D., Mach, K.J., Bilir, T.E., Chatterjee, M., Ebi, K.L., Estrada, Y.O., Genova, R.C., Girma, B., Kissel, E.S., Levy, A.N., MacCracken, S., Mastrandrea, P.R., White, L.L. (Eds.), Climate Change 2014: Impacts, Adaptation, and Vulnerability. Part B: Regional Aspects. Contribution of Working Group II to the Fifth Assessment Report of the Intergovernmental Panel on Climate Change. Cambridge University Press, Cambridge & New York.

Justic, D., Rabalais, N.N., Turner, R.E., 1996. Effects of climate change on hypoxia in coastal waters: a doubled CO_2 scenario for the northern Gulf of Mexico. Limnology and Oceanography 41, 992–1003.

Justic, D., Rabalais, N.N., Turner, R.E., 2002. Modeling the impacts of decadal changes in riverine nutrient fluxes on coastal eutrophication near the Mississippi River Delta. Ecological Modelling 153, 33–46.

Justic, D., Rabalais, N.N., Turner, R.E., 2003. Simulated responses of the Gulf of Mexico hypoxia to variations in climate and anthropogenic nutrient loading. Journal of Marine Systems 42, 115–126.

Justic, D., Rabalais, N.N., Turner, R.E., 2005. Coupling between climate variability and marine coastal eutrophication: Historical evidence and future outlook. Journal of Sea Research 54, 25–35.

Justic, D., Bierman, J.V., Scavia, D., Hetland, R., 2007. Forecasting Gulf's hypoxia: the next 50 years? Estuaries and Coasts 30, 791–801.

Justic, D., Wang, L., 2014. Assessing temporal and spatial variability of hypoxia over the inner Louisiana-upper Texas shelf: application of an unstructured-grid three-dimensional coupled hydrodynamic-water quality model. Continental Shelf Research 72, 163–179.

Kripalani, H.R., Oh, H.J., Chaudhari, S.H., 2006. Response of the East Asian summer monsoon to doubled atmospheric CO_2: coupled climate model simulations and projections under IPCC AR4. Theoretical and Applied Climatology 87, 1–28.

Kripalani, R.H., Oh, J.H., Kulkarni, A., Sabade, S.S., Chaudhari, H.S., 2007. South Asian summer monsoon precipitation variability: coupled climate model simulations and projections under IPCC AR4. Theoretical and Applied Climatology 90, 133–159.

Lachkar, Z., Gruber, N., 2011. What controls biological production in coastal upwelling systems? Insights from a comparative modeling study. Biogeosciences 8, 2,961–2,976.

Lachkar, Z., Gruber, N., 2012. Exploring the future evolution of multiple stressors in eastern boundary upwelling systems. Ocean Carbon Biogeochemistry News 5 (2), 5–9.

Lachkar, Z., Gruber, N., 2013. Response of biological production and air-sea CO_2 fluxes to upwelling intensification in the California and Canary Current systems. Journal of Marine System 109–110, 149–160.
Lachkar, Z., 2014. Effects of upwelling increase on ocean acidification in the California and Canary Current systems. Geophysical Research Letters 41, 90–95.
Lerman, A., Guidry, M., Andersson, A.J., Mackenzie, F.T., 2011. Coastal ocean last glacial maximum to 2100 CO_2-carbonic acid-carbonate system: a modeling approach. Aquatic Geochemistry 17, 749–773.
Levy, M., Klein, P., Treguier, A.M., 2001. Impact of sub-mesoscale physics on production and subduction of phytoplankton in an oligotrophic regime. Journal of Marine Research 59, 535–565.
Liu, K.K., Chao, S.Y., Shaw, P.T., Gong, G.C., Chen, C.C., Tang, T.Y., 2002. Monsoon-forced chlorophyll distribution and primary production in the South China Sea: observations and a numerical study. Deep Sea Research Part I: Oceanographic Research Papers 49, 1387–1412.
Liu, K.-K., Chao, S.-Y., Lee, H.-J., Gong, G.-C., Teng, Y.-C., 2010. Seasonal variation of primary productivity in the East China Sea: A numerical study based on coupled physical-biogeochemical model. Deep Sea Research Part II: Topical Studies in Oceanography 57, 1762–1782.
Liu, Z., Zhang, L., Cai, W.-J., Wang, L., Xue, M., Zhang, X., 2014. Removal of dissolved inorganic carbon in the Yellow River Estuary. Limnology and Oceanography 59, 413–426.
Liu, K.-K., Yan, W., Lee, H.-J., Chao, S.-Y., Gong, G.-C., Yeh, T.-Y., 2015. Impacts of increasing dissolved inorganic nitrogen discharged from Changjiang on primary production and seafloor oxygen demand in the East China Sea from 1970 to 2002. Journal of Marine Systems 141, 200–217.
McGillicuddy, D.J., Robinson, A.R., Siegel, D.A., Jannasch, H.W., Johnson, R., Dickey, T.D., McNeil, J., Michaels, A.F., Knap, A.H., 1998. Influence of mesoscale eddies on new production in the Sargasso Sea. Nature 394, 263–266.
McLeod, E., Poulter, B., Hinkel, J., Reyes, E., Salm, R., 2010. Sea-level rise impact models and environmental conservation: a review of models and their applications. Ocean and Coastal Management 53 (9), 507–517.
Meselhe, E., Reed, D.J., Grace, A.O., 2015. 2017 Coastal Master Plan: Appendix C: Modeling, Version I. Coastal Protection and Restoration Authority, Baton Rouge, Louisiana. http://coastal.la.gov/wp-content/uploads/2016/02/Appendix-C-Ch123_021716.pdf.
Mitsch, W.J., Gosselink, J.G., 2000. Wetlands. John Wiley & Sons Inc., New York.
Moisan, J.R., Hofmann, E.E., 1996. Modeling nutrient and plankton processes in the California coastal transition zone 1. A time- and depth-dependent model. Journal of Geophysical Research 101, 22647–22676.
Nagai, T., Gruber, N., Frenzel, H., Lachkar, Z., McWilliams, J.C., Plattner, G.K., 2015. Dominant role of eddies and filaments in the offshore transport of carbon and nutrients in the California Current System. Journal of Geophysical Research 120. http://dx.doi.org/10.1002/2015JC010889.
Najjar, R., Pyke, C., Adams, M.B., Breitburg, D., Hershner, C., Kemp, M., Howarth, R., Mulholland, M., Paolisso, M., Secor, D., Sellner, K., Wardrop, D., Wood, R., 2010. Potential climate-change impacts on the Chesapeake Bay. Estuarine, Coastal and Shelf Science 86, 1–20.
Natural Resource Professionals, 2011. Spanish Lake Wetland Data Report. USACE, Vicksburg, Mississippi.
Osterman, L.E., Poore, R.Z., Swarzenski, P.W., 2008. The last 1000 years of natural and anthropogenic low oxygen bottom water on the Louisiana Shelf Gulf of Mexico. Marine Micropaleontology 66, 291–303.
Osterman, L.E., Poore, R.Z., Swarzenski, P.W., Senn, D.B., DiMarco, S.F., 2009. The 20th-century development and expansion of Louisiana shelf hypoxia. Geo-Marine Letters 29, 405–414.
Pauly, D., Christensen, V., 1995. Primary production required to sustain global fisheries. Nature 374, 225–257.
Peyronnin, N., Green, M., Richards, C.P., Owens, A., Reed, D., Chamberlain, J., Groves, D.G., Rhinehart, W.K., Belhadjali, K., 2013. Louisiana's 2012 coastal master plan: overview of a science-based and publicly informed decision-making process. Journal of Coastal Research 67 (sp1), 1–15.
Rabalais, N.N., Turner, R.E., 2001. Hypoxia in the northern Gulf of Mexico: description, causes and change. In: Rabalais, N.N., Turner, R.E. (Eds.), Coastal Hypoxia: Consequences for Living Resources and Ecosystems, Coastal and Estuarine Studies, vol. 58. American Geophysical Union, Washington, D.C, pp. 1–36.
Rabalais, N.N., Turner, R.E., Sen Gupta, B.K., Boesch, D.F., Chapman, P., Murrell, M.C., 2007. Hypoxia in the northern Gulf of Mexico: does the science support the plan to reduce, mitigate, and control hypoxia? Estuaries and Coasts 30, 753–772.
Rabalais, N.N., Turner, R.E., Diaz, R.J., Justic, D., 2009. Global change and eutrophication of coastal waters. ICES Journal of Marine Science 66, 1528–1537.

Rabalais, N.N., Diaz, R.J., Levin, L.A., Turner, R.E., Gilbert, D., Zhang, J., 2010. Dynamics and distribution of natural and human-caused hypoxia. Biogeosciences 7, 585–619.

Ren, W., Tian, H., Tao, B., Yang, J., Pan, S., Cai, W.J., Lohrenz, S.E., He, R., Hopkinson, C.S., 2015. Large increase in dissolved inorganic carbon flux from the Mississippi River to Gulf of Mexico due to climatic and anthropogenic changes over the 21st century. Journal of Geophysical Research: Biogeosciences 120, 724–736.

Rogers, K., Saintilan, N., Copeland, C., 2012. Modelling wetland surface elevation dynamics and its application to forecasting the effects of sea-level rise on estuarine wetlands. Ecological Modelling 244, 148–157.

Rose, K.A., Adamack, A.T., Murphy, C.A., Sable, S.E., Kolesar, S.E., Craig, J.K., Breitburg, D.L., Thomas, P., Brouwer, M.H., Cerco, C.F., Diamond, S., 2009. Does hypoxia have population-level effects on coastal fish? Musings from the virtual world. Journal of Experimental Marine Biology and Ecology 381, S188–S203.

Rose, K.A., Allen, J.I., 2013. Modeling marine ecosystem responses to global climate change: where are we now and where should we be going? Ecological Modelling 264, 1–6.

Rose, K.A., Fiechter, J., Curchitser, E.N., Hedstrom, K., Bernal, M., Creekmore, S., Haynie, A., Ito, S., Lluch-Cota, S., Megrey, B.A., Edwards, C., Checkley, D., Koslow, T., McClatchie, S., Werner, F., 2015. Demonstration of a fully-coupled end-to-end model for small pelagic fish using sardine and anchovy in the California Current. Progress in Oceanography 138, 348–380.

Ruzicka, J.J., Brink, K.H., Gifford, D.J., Bahr, F., 2016. A physically coupled end-to-end model platform for coastal ecosystems: Simulating the effects of climate change and changing upwelling characteristics on the Northern California Current ecosystem. Ecological Modelling. http://dx.doi.org/10.1016/j.ecolmodel.2016.01.018.

Rykaczewski, R.R., Dunne, J.P., 2010. Enhanced nutrient supply to the California current ecosystem with global warming and increased stratification in an earth system model. Geophysical Research Letters 37, L21606.

Sasser, C.E., Gosselink, J.G., Swenson, E.M., Swarzenski, C.M., Leibowitz, N.C., 1996. Vegetation, substrate and hydrology in floating marshes in the Mississippi river delta plain wetlands, USA. Vegetatio 122 (2), 129–142.

Seitzinger, S.P., Harrison, J.A., Dumont, E., Beusen, A.H.W., Bouwman, A.F., 2005. Sources and delivery of carbon, nitrogen, and phosphorus to the coastal zone: an overview of Global Nutrient Export from Watersheds (NEWS) models and their application. Global Biogeochemical Cycles 19, GB4S01. http://dx.doi.org/10.1029/2005GB002606.

Shchepetkin, A.F., Mcwilliams, J.C., 2005. The Regional Ocean Modeling System (ROMS): a split-explicit, free-surface, topography-following coordinates ocean model. Ocean Modelling 9, 347–404.

Skamarock, W.C., Klemp, J.B., Dudhia, J., Gill, D.O., Barker, D.M., Wang, W., et al., 2005. A Description of the Advanced Research WRF Version 2. Technical Note, NCAR/TN-468+STR. NCAR.

Snedden, G.A., Steyer, G.D., 2013. Predictive occurrence models for coastal wetland plant communities: Delineating hydrologic response surfaces with multinomial logistic regression. Estuarine. Coastal and Shelf Science 118, 11–23.

Sperna Weiland, F.C.,L.P.H., van Beek, L.P.H., Kwadijk, J.C.J., Bierkens, M.F.P., 2012. Global patterns of change in discharge regimes for 2100. Hydrology and Earth System Sciences 16, 1047–1062.

Spitz, Y.H., Newberger, P.A., Allen, J.S., 2003. Ecosystem response to upwelling off the Oregon coast: Behavior of three nitrogen-based models. Journal of Geophysical Research 108 (C3), 3062.

Storlazzi, C.D., Elias, E., Field, M.E., Presto, M.K., 2011. Numerical modeling of the impact of sea-level rise on fringing coral reef hydrodynamics and sediment transport. Coral Reefs 30, 83–96.

Sydeman, W.J., Garcia-Reyes, M., Schoeman, D.S., Rykaczewski, R.R., Thompson, S.A., Black, B.A., Bograd, S.J., 2014. Climate change and wind intensification in coastal upwelling ecosystems. Science 345, 77–80.

Syvitski, J.P.M., Kettner, A.J., Overeem, I., Hutton, E.W.H., Hannon, M.T., Brakenridge, G.R., et al., 2009. Sinking deltas due to human activities. Nature Geosciences 2, 681–686.

Tebaldi, C., Strauss, B.H., Zervas, C.E., 2012. Modeling sea level rise impacts on storm surges along US coasts. Environmental Research Letters 7, 014032. http://dx.doi.org/10.1088/1748-9326/7/1/014032.

Theriot, R.F., 1993. Flood Tolerance of Plant Species in Bottomland Hardwood Forests of the Southeastern United States. Wetland Research Program Technical Report WRP-DE-6.

Turner, R.E., Rabalais, N.N., 1994. Evidence for coastal eutrophication near the Mississippi river delta. Nature 368, 619–621.

Turner, A.G., Annamalai, H., 2012. Climate change and the South Asian summer monsoon. Nature Climate Change 2, 587–595.

Turner, R.E., Rabalais, N.N., Justic, D., 2012. Predicting summer hypoxia in the northern Gulf of Mexico: Redux. Marine Pollution Bulletin 64, 319–324.

Visser, J.M., Duke-Sylvester, S.M., Carter, J., Broussard III, W.P., 2013. A computer model to forecast wetland vegetation changes resulting from restoration and protection in coastal Louisiana. Journal of Coastal Research 67 (sp1), 51–59.

Visser, J.M., Duke-Sylvester, S.M., Shaffer, G.P., Hester, M.W., Couvillion, B., Broussard III, W.P., Willis, J., Beck, H., 2015. 2017 Coastal Master Plan: Model Improvement Plan, Additional Vegetation Communities (Subtask 4.4), Version I. Coastal Protection and Restoration Authority, Baton Rouge, Louisiana.

Wall, D.P., Darwin, S.P., 1999. Vegetation and elevation gradients within a bottomland hardwood forest of southeastern Louisiana. American Naturalist 142 (1), 17–30.

Wang, B., Wu, R., Fu, X., 2000. Pacific-East Asia teleconnection: how does ENSO affect East Asian Climate. Journal of Climate 13, 1517–1536.

Wang, S., McGrath, R., Hanafin, J., Lynch, P., Semmler, T., Nolan, P., 2008. The impact of climate change on storm surges over Irish waters. Ocean Modelling 25 (1–2), 83–94.

Wang, L., Justic, D., 2009. A modeling study of the physical processes affecting the development of seasonal hypoxia over the inner Louisiana-Texas shelf: Circulation and stratification. Continental Shelf Research 9, 1464–1476.

Wang, H.J., Saito, Y., Zhang, Y., Bi, N.S., Sun, X.X., Yang, Z.S., 2011. Recent changes of sediment flux to the western Pacific Ocean from major rivers in East and Southeast Asia. Earth-Science Reviews 108, 80–100.

Wang, D., Gouhier, T.C., Menge, B.A., Ganguly, A.R., 2015. Intensification and spatial homogenization of coastal upwelling under climate change. Nature 518, 390–394.

Warner, J.C., Armstrong, B., He, R., Zambon, J.B., 2010. Development of a Coupled Ocean-Atmosphere-Wave-Sediment Transport (COAWST) modeling system. Ocean Modeling 35, 230–244.

Xu, M., Xu, H., Ma, J., 2015. Responses of the East Asian winter monsoon to global warming in CMIP5 models. International Journal of Climatology. http://dx.doi.org/10.1002/joc.4480.

Xue, Z., He, R., Liu, J.P., Warner, J.C., 2012. Modeling transport and deposition of the Mekong River sediment. Continental Shelf Research 37, 66–78.

Zeng, X., He, R., Xue, Z., Wang, H., Wang, Y., Yao, Z., et al., 2015. River-derived sediment suspension and transport in the Bohai, Yellow, and East China Seas: A preliminary modeling study. Continental Shelf Research 111 (Part B), 112–125.